Improved Return Passages for Multistage Centrifugal Compressors

by

Benjamin W. Glass

B.S. Aeronautics and Astronautics
Massachusetts Institute of Technology, 2008

Submitted to the Department of Aeronautics and Astronautics
in partial fulfillment of the requirements for the degree of

Master of Science in Aeronautics and Astronautics

at the

MASSACHUSETTS INSTITUTE OF TECHNOLOGY

September 2010

Author.....
Department of Aeronautics and Astronautics
August 19, 2010

Certified by.....
Edward M. Greitzer
H. N. Slater Professor of Aeronautics and Astronautics
Thesis Supervisor

Accepted by.....
Eytan H. Modiano
Associate Professor of Aeronautics and Astronautics
Chair, Committee on Graduate Students

Improved Return Passages for Multistage Centrifugal Compressors

by

Benjamin W. Glass

Submitted to the Department of Aeronautics and Astronautics
on August 19, 2010, in partial fulfillment of the
requirements for the degree of
Master of Science in Aeronautics and Astronautics

Abstract

This thesis presents a design concept for return passages in multistage centrifugal compressors. Flow in a baseline return passage is analyzed to identify loss sources that have substantial potential for reduction. For the geometry analyzed, it is found that mismatched incidence of the return vane, separation on the hub surface at the exit of the return bend, and blockage due to separation on the shroud surface near the return bend inlet lead to losses which have such potential. Preliminary designs were developed and computationally assessed to determine effective geometries for eliminating separation on the hub at the return bend exit and for reducing losses. Then, based on assessment of the preliminary designs, other features of the loss generation were addressed. The geometry proposed includes an increased axial extent of the return bend, an increasing radius of curvature through the return bend, and lean of the return vane leading edge, mitigating the loss mechanisms identified in the baseline return passage. The three-dimensional calculations showed a cumulative loss coefficient that was 10% lower than the baseline.

The design described was carried out with a fixed inlet condition, and a second return passage was thus developed to determine the potential loss reduction if the inlet geometry were modified. (The design of the impeller required to achieve the modified inlet flow was not considered.) The cumulative loss coefficient was reduced by 27% compared with the baseline, with the implication that an area for exploration is integration of the impeller and return passage flow fields.

Thesis Supervisor: Edward M. Greitzer
Title: H.N. Slater Professor of Aeronautics and Astronautics

Acknowledgments

I am most grateful to my advisor, Professor Greitzer, for his support and encouragement, and his unfailing willingness and desire to teach. My time as a graduate student in the Gas Turbine Lab was an incredible learning experience, due in large part to Professor Greitzer's insistence that I take away the intellectual nugget from each step of the process.

I would also like to thank Mitsubishi Heavy Industries, Ltd., and specifically Dr. Sumiu Uchida, for their support of this thesis and their interest and interactions.

At MIT, I am deeply indebted to Professor Zoltán Spakovzky for his continuous support throughout this project. His insight and advice was invaluable, as was his presence at MHI. I am also thankful for the experience and wisdom that Dr. Choon Tan shared as I became familiar with CFD techniques.

Outside of MIT, I am very grateful to Dr. Mick Casey, of the University of Stuttgart, who lent his considerable experience with centrifugal compressors to the project. Professor Nick Cumpsty of Imperial College also provided invaluable feedback during his frequent visits to the GTL.

Without the incredible patience and endless technical assistance of my fellow graduate student and GTL network administrator, Jeff Defoe, the computational aspects of my research would have gone nowhere, and for this reason I am particularly grateful to Jeff. I would also like to thank fellow graduate students Jon Everitt, Andreas Peters, Dave Hall, Sean Nolan, Hiten Mulchandi, Metodi Zlatinov and everyone else at the GTL for the many discussions we shared, both on and off the topic of our research.

Finally, I am incredibly thankful for the love and support of my parents, grandparents and sister. While they didn't always understand the work I was doing, they always encouraged me to work hard and enjoy life.

Contents

List of Figures

List of Tables

Nomenclature

Abbreviations

CAD	Computer Aided Drafting
CFD	Computational Fluid Dynamics
MHI	Mitsubishi Heavy Industries
RANS	Reynolds-Averaged Navier-Stokes
SST	Shear Stress Transport

Roman Symbols

A	area
b	passage width
d	diameter
k	turbulent kinetic energy
k	thermal conductivity
l	non-dimensional meridional distance
$\dot{m}$	mass flow
P	pressure
$\dot{Q}_0$	inlet stagnation volume flow rate
r	radius
S	entropy
$\dot{S}$	volumetric entropy production rate
T	temperature

u	velocity
U	impeller tip speed
V	velocity
Y^+	non-dimensional wall distance

Greek Symbols

Φ	flow coefficient
ρ	density
τ_{ij}	viscous stress
ω	specific dissipation rate
Ω	rotational speed
ζ	loss coefficient

Subscripts

$base$	baseline return passage
d	design condition
FD	FD series return passage
i, j	index
n	normal to diffuser inlet
r	radial
ref	reference quantity
t	stagnation quantity
s	parallel to diffuser inlet
t	tangential
z	axial
0	stage inlet
2	diffuser inlet
θ	tangential

Chapter 1

Introduction

This thesis described the development of design concepts for improved performance of multistage centrifugal compressor return passages. These return passages are necessary to obtain high efficiency in compact centrifugal compressors. The design must deal with high kinetic energy in the return passage which leads to increased losses.

1.1 Background and Motivation

Multistage centrifugal compressors are employed in a wide range of applications in the oil & gas and chemical processing industries. Discharge pressures range from 10-20 bar in ethylene cracked gas compressors up to 600 bar in oil field reinjection compressors [1]. Centrifugal compressors have fewer moving parts and require less maintenance than alternatives such as reciprocating compressors, which are also used in the process industries.

The first successful single-shaft, multistage centrifugal compressor produced an output pressure of 1.45 bar from 5 stages in 1905 [1]. Since then multistage centrifugal compressors have progressed to single stage pressure ratios exceeding 8:1. Efficiency has also increased roughly $^2/_3$ per cent per year [2] . Much of the development effort has gone into refining the impeller, and impellers have progressed from simple two-dimensional blades to sophisticated, three-dimensional designs [3].

Historically, radial diffusers with diffusion ratios (ie. ratio of diffuser outlet radius

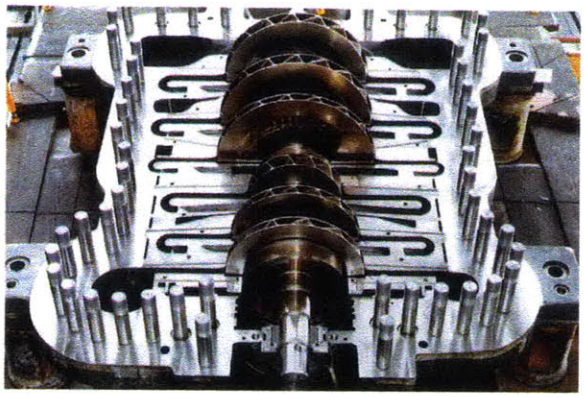

Figure 1-1: Horizontally-split multistage centrifugal compressor.

to diffuser inlet radius) up to 2 have been used to slow the flow exiting the impeller. The large radius at the exit of the diffuser meant the kinetic energy, and thus the losses, in the return bend and return vane were small compared with the impeller losses. However, to meet the demands of the oil & gas industry, process compressor manufacturers have focused on reducing compressor cost and increasing reliability. The mass, and cost, of the compressor casing scales roughly with the square of the maximum radius of the return passage. As such the maximum casing radius is a key driver for compressor cost and radially compact designs are an aspect of interest.

Single-shaft multistage centrifugal compressors can have over 6 impellers on a single shaft, with bearings on either end, as shown in Figure 1-1. Long shafts can lead to increased vibration and wearing of the labyrinth seals. Designers thus seek to increase shaft stiffness by employing axially compact stages with increased shaft diameter.

Compressor development has relied to a large extent on modifications of existing designs. Such modifications, especially of the return passage, are based on experimental data from standard stage designs, with the goal of achieving higher efficiency compact compressors [3]. As impeller efficiencies continue to rise, and diffuser ratios drop, losses in the return passage become more critical to overall stage performance. To achieve an improvement in return passage performance, this thesis explores a number of new design concepts which may be used to increase efficiency, improve reliability and decrease the cost of multistage centrifugal compressors.

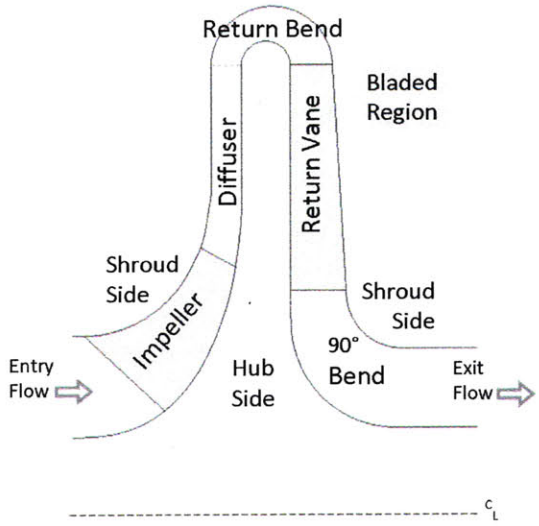

Figure 1-2: Components of a typical centrifugal compressor stage with a vaneless diffuser.

1.1.1 Return Passage Geometry

The centrifugal compressor can be divided into five components. In flow order, the components are the impeller, diffuser, return bend, return vane and 90° bend. The impeller and return channel components include blades and vanes, respectively. The hub side of the passage is radially inward and adjacent to the compressor shaft, and the shroud side is radially outward. A schematic of the components of a centrifugal compressor stage is shown in Figure 1-2. Flow enters at the left and exits at the right. The wall contours are different for subsequent designs described in sections 4 and 5, but the minimum and maximum radius of each component is maintained from baseline.

1.2 Previous Work

In the 1980's, a number of experiments were carried out to analyze the flow in return passages and optimize the design of return passages. Simon and Rothstein [4] found a strong adverse pressure gradient, and resulting separation, on the latter half of the return bend hub in a stage with flow coefficient Φ=0.153, defined as the volume flow

rate over the product of the impeller frontal area and the impeller tip speed, and a radius of curvature in the bend $r/d_2 = 0.075$. The adverse pressure gradient was relieved by increasing the radius of curvature in the bend to $r/d_2 = 0.15$. Inoue and Koizumi [5] showed that for diffuser inlet flow angles less than 30° from tangential, there was a variation in stagnation pressure and flow angle across the span at the exit of the diffuser, as well as reverse flow on the shroud. At the exit of the return bend the flow was fully attached and the stagnation pressure and flow angle are nearly constant across the span. Inoue and Koizumi conclude that three-dimensional return vanes, with leading edge lean and twist, are not necessary. Several non-traditional geometries were also tested, including an axially extended return bend with diffuser vanes [6], and a "continuous diffusion" return passage [7]. No general conclusions were put forward regarding an optimal design.

Fister, et. al. developed a numerical method for calculating the flow in return passages [8]. They described satisfactory agreement with experiment, but the computational method was restricted to flows without separation to reduce the required computer time. Their method is thus not applicable to typical centrifugal compressor return passages which have regions of separation.

More recently Lenke and Simon [9] compared the calculated flow field in the flow coefficient Φ=0.009 stage geometry that Simon and Rothstein tested in 1983[4] using a Reynolds stress turbulence model and a k-ε turbulence model. Both turbulence models showed a separation region on the suction side of the return vane at design point. In their words, the calculated losses were very similar with both turbulence models, and the difference was not quantified.

In a comprehensive return passage redesign effort, Aalburg et al. developed reduced loss return passages with a diffusion ratio of 1.3 and 1.19, an 8% and 14% decrease from the baseline compressor [10]. The maximum radius of the baseline return passage was first reduced without other modifications to the hub and shroud walls, except for removing the sharp corner in the bend on the shroud side. The return vane leading and trailing edge locations, leading and trailing edge lean angles, blade camberline and blade thickness distribution was then optimized using computational

Design-of-Experiments integrated with a three-dimensional Navier-Stokes solver.

Measurements showed the larger of the two redesigned return passages, with a diffusion ratio of 1.3, achieved the same peak efficiency as baseline but had roughly 3% lower efficiency at $\Phi/\Phi_d = 1.15$. The return passage with diffusion ratio 1.19 showed reduced efficiency for all flow coefficients tested. A second design optimization was performed, with modifications to the return bend diffusion ratio. Peak polytropic stage efficiency was increased by approximately 1.5 points from baseline with no decrease in operating range for the diffusion ratio 1.3 return passage, compared with baseline, showing that reduced radius return passages are feasible.

Aalburg et al. sought to further improve the performance of reduced radius return passages with diffusion ratio as low as 1.19 by extending the return vane leading edge upstream across the return bend[11]. The new return vanes resemble a boomerang and are thus called "boomerang" type return vanes. A geometry generator was developed for producing such "boomerang" return vanes with a specified blade loading. The geometry generator used an inverse design method similar to that described by Veress and Van den Braembussche [12]. Though the tangential component of the velocity, and thus the velocity magnitude, was reduced in the bend by the "boomerang" return vane the losses in the bend increased due to increased wetted area. Predicted overall losses decreased at design point, corresponding to an increase in polytropic stage efficiency of approximately 0.5-1 points. Though their conclusions were not experimentally assessed, the calculations of Aalburg et al. implied a potential for improved performance in reduced radius centrifugal compressors with return vanes which are extended upstream of the return bend.

1.3 Research Questions

In this thesis a new design concept for return passages in compact centrifugal compressor stages is developed, based on detailed investigation of the baseline return passage flow field. The design space was constrained such that the return passage could be manufactured but there was no explicit consideration of manufacturing cost.

The thesis seeks to answer the following research questions:

1. What loss mechanisms are present in the baseline return passage?

2. What effect do changes to the hub and shroud wall geometry have on the detrimental flow features observed in the baseline return passage?

3. Can reduced losses in the return passage be achieved through redesign of the return passage without modification to the impeller?

4. Can modification of the impeller result in further reduction in return passage losses, above and beyond those achievable through a redesign of the return passage alone?

1.4 Thesis Contributions

- Loss mechanisms in compact return passages are characterized. Means of alleviating these losses are developed.

- A new design concept for improved performance compact return passages is defined.

Chapter 2

Approach and Implementation

2.1 Technical Approach

To address the research questions of section 1.3 the technical approach shown in Figure 2-1 was followed. The effort was divided into two phases. In phase 1 the baseline configuration was assessed. In phase 2 the concept for improved performance return passages was developed.

2.1.1 Phase 1: Baseline Return Passage Assessment

The return passage inlet and outlet geometry and boundary conditions were kept the same for all calculations, based on three-dimensional Reynolds-Averaged Navier-Stokes (RANS) calculations of the baseline inlet, impeller and diffuser. Though the focus of this thesis is not operating range, the baseline calculations were done for flow coefficients from $\Phi/\Phi_d = 0.89$ to $\Phi/\Phi_d = 1.17$ to provide insight into off-design performance. To reduce the computational time and resources required, steady state calculations were done for a single flow passage for the impeller and for the return passage. The flow was circumferentially averaged at a mixing plane location 20% of the impeller exit width upstream of the impeller exit. This mixing plane location was taken as the diffuser inlet for subsequent calculations of the return passage, and the circumferentially averaged flow profiles at this station were used as diffuser inlet

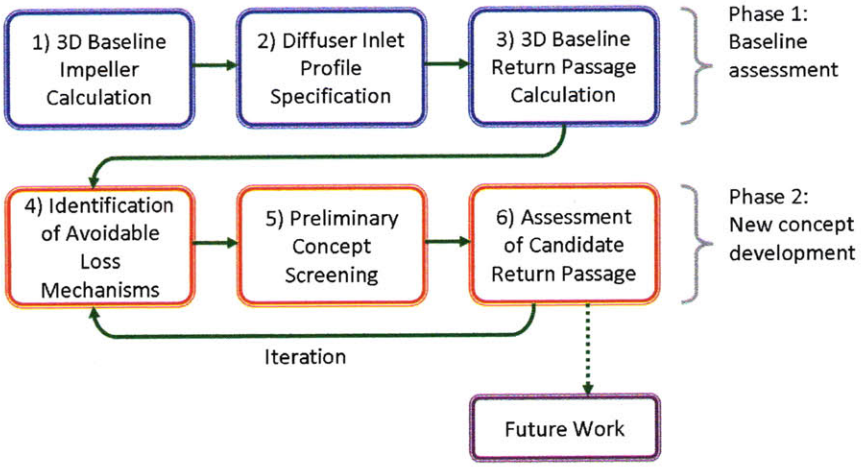

Figure 2-1: Technical approach.

boundary conditions.

The calculations of the baseline return passage, including diffuser, return bend, return vane and 90° bend, covered flow coefficients from $\Phi/\Phi_d = 0.89$ to $\Phi/\Phi_d = 1.17$. Detailed interrogation of the flow field focused on the design point, though the high and low flow coefficient cases (ie., $\Phi/\Phi_d = 1.17$ and $\Phi/\Phi_d = 0.89$, respectively) were checked to ensure no separation developed at the off-design conditions. Flow processes and loss mechanisms were investigated using both overall measures (e.g. loss coefficient, ζ) and local measures (e.g. contours of velocity components.) Loss coefficient was calculated for each component, but the effect of flow processes in each component on flow and losses in the other components was also considered.

2.1.2 Phase 2: Design Concept Development

Phase 2 encompassed the iterative design procedure for new concepts for return passages. The objectives were defined to alleviate loss mechanisms in previous return passages. Preliminary designs were screened using axisymmetric Navier-Stokes calculations. The axisymmetric calculations do not include the effect of the return vane blades but they are a useful tool for screening a large number preliminary designs. Beneficial aspects of preliminary designs were combined to develop candidate return passage meridional geometry. Axisymmetric calculations of flow angle at the leading

edge radial location in the candidate design were used to define the leading edge lean angle of the three-dimensional return vane. A detailed examination of the flow in the candidate design was then performed based on a three-dimensional Navier-Stokes calculation.

This thesis describes two design iterations using the baseline diffuser inlet geometry. Lessons learned from the first iteration were applied in the second iteration to improve the candidate return passage performance. The thesis also describes the development of a further concept which builds on the above-mentioned work, but allows the diffuser inlet geometry and flow to be modified.

2.2 Computational Methodology

2.2.1 Numerical Code

Numerical simulations were performed using ANSYS FLUENT, a commercially available CFD code. FLUENT V6.3 was used for calculations of the baseline impeller and return passage flow fields, after which the next version, FLUENT V12.0, was used. Both versions use a viscous, compressible, steady RANS solver. A rotating reference frame was used for the impeller blade region in the baseline impeller calculations. All other calculations used stationary reference frames. To reduce the computational time the three-dimensional calculations were performed on a single passage with periodic boundary conditions. For the baseline impeller calculations, a first order discretization was used to reduce computation time and improve numerical stability. Second order discretization was used for all return passage calculations in which improved accuracy was desired.

The calculations used the two-equation k-ω SST model developed by Menter [13]. The k-ω SST turbulence model transitions between near wall turbulence equations and free stream turbulence equations to describe the turbulence in both regions. The low-Reynolds formulation used in all return passage calculations provides full resolution of the boundary layer assuming the grid has a non-dimensional wall distance,

Y^+, roughly equal to one[14]. While the k-ω SST turbulence model is suggested as appropriate for swirling flows such as those in centrifugal compressor return passages[1], there are known deficiencies. For example, the model does not account for the stabilizing effect of increased turbulent mixing near concave surfaces [15, 16].

2.2.2 Mesh Generation and Adaptation

Initial structured grids for each calculation were created using the commercial gridding software Pointwise®. The geometry for the baseline impeller and return passage grids were provided by MHI. Geometry for remaining grids was generated using a variety of CAD and geometry definition software and imported into the Pointwise® environment. A C-grid topology was used for the impeller blades, which have a blunt trailing edge. All return vane grids were based on an O-grid topology. The impeller grid and a typical return vane grid are shown in Figure 2-2 and Figure 2-3. Before adapting the grid, the spacing on the return passage blade and passage walls was $< 0.0003b_2$, or under 0.03% of the diffuser inlet passage width, to ensure compatibility with the low-Reynolds number formulation of the k-ω SST turbulence model. Initial grid spacing was $< 0.009b_2$ for the impeller calculations which used the standard k-ω SST turbulence model.

An initial solution for each case was calculated on the structured grid created with Pointwise®. The built-in grid adaptation feature in ANSYS FLUENT was used to further adapt the grid based on the Y^+ value in a preliminary solution calculated with the initial grid. Each return passage grid was refined to ensure $Y^+ \approx 1$. The final cell count for each set of calculations is given in Table 2.1. [2]

2.2.3 Upstream Influence of Return Vane

To assess the use of axisymmetric calculations without return vane blades for screening preliminary return passage designs, the upstream influence of the return vane blades

[1]Personal communication with Dr. M. V. Casey

[2]The smaller cell count of the new return passage grids relative to the baseline return passage grid reflects the improvement in the author's grid generation and adaptation skills.

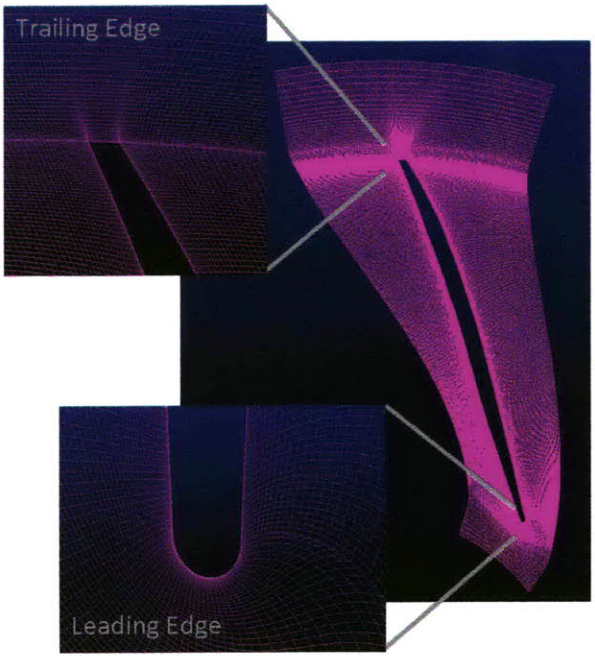

Figure 2-2: C-grid topology used in impeller grid.

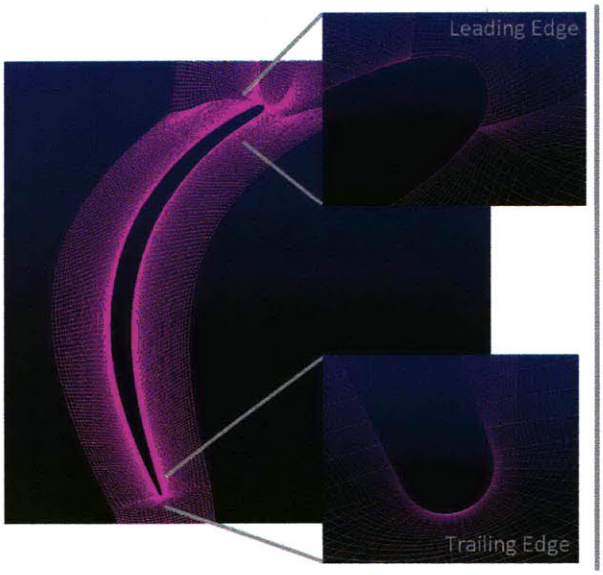

Figure 2-3: Typical return vane grid.

Table 2.1: Cell count of grids used.

Grid	Cell Count
Baseline impeller grid	4.63M
Baseline return passage grid	3.25M
New return passage grids	~2.2M
Axisymmetric return passage grids	~14K

on the static pressure field was examined. A comparison of the flow field from three-dimensional and axisymmetric calculations of the same meridional geometry show separation on the hub at the exit of the return bend. Static pressure distributions are visually uniform in the pitch direction in the diffuser or the first half of the return bend. A more detailed description of the upstream decay of the return vane blade pressure field is provided in Appendix A.

2.2.4 Performance Metrics

The operating condition of the compressor stage is given by the flow coefficient, Φ. While several definitions of flow coefficient exist, we have adapted that used by MHI, calculated as

$$\Phi = \frac{\dot{Q}_0}{\frac{\pi}{4} d_2^2 U_2}, \tag{2.1}$$

where d_2 is the mean impeller tip diameter, U_2 is the impeller tip speed, and $\dot{Q}_0$ is the inlet stagnation volume pressure flow rate, calculated as

$$\dot{Q}_0 = \frac{\dot{m}}{\rho_{t0}}. \tag{2.2}$$

The loss coefficient, ζ , provides a quantitative measure of the performance of a flow passage. Loss coefficient is used in this thesis as a performance metric for the return passage. The loss coefficient for a component is defined as:

$$\zeta = \frac{P_{t,upstream} - P_{t,downstream}}{(1/2 \rho_2 V_2^2)_{ref}}. \tag{2.3}$$

In equation 2.3 the values of P_t are mass-weighted at the upstream and downstream stations which define the selected component or components of the return passage.

In the calculation of overall loss coefficient, the upstream station is the diffuser inlet and the downstream station is the return passage outlet. The reference quantities are calculated at the diffuser inlet to allow direct comparison between the loss coefficients of different components. The relation between changes in return passage loss coefficient and polytropic stage efficiency for a stage with pressure ratio of roughly 2, which is representative of the configuration examined, is shown in Figure 2-4

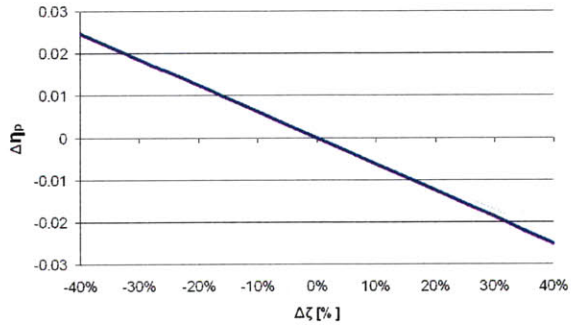

Figure 2-4: Changes in polytropic stage efficiency versus changes in return passage loss coefficient.

The loss coefficient satisfactorily describes the losses in the return passage, and can be used to compare the performance of individual components of the return passage. However, it does not give information about the flow processes which lead to stagnation pressure losses and entropy rise. To characterize these flow processes velocity components were displayed to identify separation regions and other flow features. Cell-by-cell graphical display of volumetric entropy production was also used to indicate areas of high losses. For each cell in the grid, the volumetric entropy production, $\dot{S}$, was calculated as[17]:

$$\dot{S} = \frac{k}{T^2}(\frac{\partial T}{\partial x_i})^2 + \frac{\tau_{ij}}{T}\frac{\partial u_i}{\partial x_j}. \tag{2.4}$$

The first term in the right-hand-side of equation 2.4 is the entropy produced from heat transfer and the second term is the viscous dissipation. k and τ_{ij} are the turbulent thermal conductivity and viscous stress, respectively. With $Y^+ \approx 1$, the integrated cell-by-cell entropy production in the return passage is within 10% of the difference

in entropy flux between the return passage outlet and inlet. Calculation of entropy production gives information about where in the flow high losses are produced and is a useful tool for assessing candidate designs.

Volumetric entropy production due to mixing of secondary flows is typically several orders of magnitude lower than volumetric entropy production in the boundary layer. However, the region in which mixing losses occur can be several orders of magnitude larger than the volume of the boundary layer, and thus the mixing losses are an important source of entropy production. To effectively display the volumetric entropy production in the boundary layer and in regions where mixing takes place, the volumetric entropy production is plotted on a log scale, and is normalized by the volume-weighted volumetric entropy production in the baseline return passage, $\dot{S}_{baseline}$.

2.3 Derivation of Diffuser Inlet Profile from Calculation of Baseline Impeller

In the first two steps of the technical approach in section 2.1 boundary conditions for the return passage calculations are specified. The mass flow and circumferentially-averaged profiles of flow variables at the inlet to the diffuser domain are defined based on calculation of the flow field in the baseline impeller. These boundary conditions are used for subsequent return passage calculations, both the baseline return passage and the new return passage concepts.

The procedure for defining the boundary conditions is as follows:

1. Calculate flow field in impeller.

2. Output flow file at mixing plane location.

3. Calculate circumferentially "mixed out" average of flow at mixing plane (using MatLab script) and write input file for use in FLUENT.

4. Use radial flow profile file (from MatLab script) as input to FLUENT return passage calculations.

The mixing plane model in step 3 is described below.

2.3.1 Mixing Plane Model

It is common practice to employ a mixing plane model to simplify the calculation of multi-blade row turbomachinery[18]. The mixing plane removes the circumferential unsteadiness of the flow, permiting calculation of the downstream passage using steady-state solvers. The time accurate flow in a radial diffuser has been shown to be qualitatively similar to the time-averaged flow. Calculation of losses from the unsteady case and the steady case showed only a 5% difference[19]. The bulk of the losses in the radial diffuser are due to the spanwise variation in incidence angle at diffuser inlet, and thus are captured by the mixing plane model. For this thesis, the loss in fidelity is acceptable given the simplification provided by the mixing plane model.

2.3.1.1 Circumferentially "Mixed Out" Averaging

To capture the losses produced in the mixing process in the vaneless diffuser, a "mixed out" average using conservation of momentum, mass and energy was used. The mixed out average assumes complete mixing of the flow at constant area.

The mixing plane coordinate system was chosen to simplify the conservation equations. The $\hat{\theta}$ and $\hat{n}$ axes are tangential and normal to the impeller exit plane, respectively, and the third axis, $\hat{s}$, is parallel to the impeller exit in the r-z plane. A schematic of the region near the impeller exit in the r-z plane is shown in 2-5. The $\hat{n}$ and $\hat{s}$ axes are shown and the $\hat{\theta}$ axis is out of the page. As described in section 2.3.1.3, the mixing plane, indicated by a red line, is located 20% of the impeller exit width downstream of the impeller exit, indicated by a blue line.

The conservation equations which define the mixed out average are given in equa-

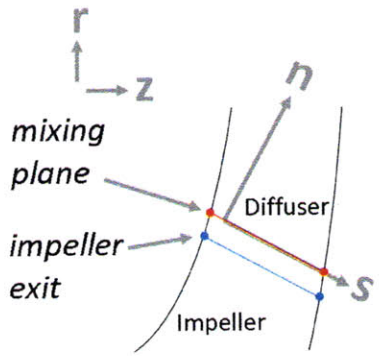

Figure 2-5: Schematic (in r-z plane) of region near the impeller exit (blue line) shows the mixing plane (red line) and the $\hat{n}$ and $\hat{s}$ axes of the mixing plane coordinate system.

tions 2.5 through 2.9 [20].

$$mass : \sum(\rho_i V_{n_i} A_i) = \bar{\rho}\bar{V}_n A \tag{2.5}$$

$$energy : \sum(T_{t_i}\rho_i V_{n_i} A_i) = \bar{T}_t \dot{m} \tag{2.6}$$

$$\hat{n} - momentum : \sum(\rho_i V_{n_i}^2 A_i + P_i A_i) = \bar{\rho}\bar{V}_n^2 A + \bar{P}A \tag{2.7}$$

$$\hat{s} - momentum : \sum(V_{s_i}\rho_i V_{n_i} A_i) = \bar{V}_s\bar{\rho}\bar{V}_n A \tag{2.8}$$

$$\hat{\theta} - momentum : \sum(V_{\theta_i}\rho_i V_{n_i} A_i) = \bar{V}_\theta\bar{\rho}\bar{V}_n A \tag{2.9}$$

The circumferentially averaged turbulent kinetic energy, k, and specific dissipation, ω, are calculated using a mass-averaging technique as

$$\frac{\int \phi\rho \left|\vec{V}\cdot d\vec{A}\right|}{\int \rho \left|\vec{V}\cdot d\vec{A}\right|} = \frac{\sum_{i=1}^{n} \phi_i\rho_i \left|\vec{V}_i\cdot \vec{A}_i\right|}{\sum_{i=1}^{n} \rho_i \left|\vec{V}_i\cdot \vec{A}_i\right|}, \tag{2.10}$$

where ϕ is replaced with k or ω [14].

2.3.1.2 MatLab Implementation

The mixing plane model was implemented in MatLab. A MatLab script was written to extract flow field data on a structured boundary surface from a point profile file (*.prof*) which is created in FLUENT. The script calculates the circumferentially averaged values of $P, P_t, T_t, V_r, V_z, V_\theta$, k and ω and creates a new axial or radial profile file to be read into three-dimensional or axisymmetric FLUENT calculations, respectively.

2.3.1.3 Mixing Plane Location

The mixing plane location was chosen to ensure no regions of reverse flow. A region of reverse flow on the impeller shroud which extends beyond 20% of the impeller exit width, b_2, into the diffuser is present in the impeller calculations. Figure 2-6 shows contours of radial velocity for the lowest flow coefficient, $\Phi/\Phi_d = 0.84$, in the ϑ-z plane at four radial stations, from the impeller exit at left to 20% of the impeller exit width, or $0.2b_2$, downstream of the impeller exit at right. Contours are only shown where there is reversed flow. The radial velocity contours are overlaid on the impeller hub wall, shroud wall mid-pitch line and impeller blade trailing edge geometry. The region of reverse flow is smallest at the $0.2b_2$ station and is largest at the impeller exit. To prevent an ill-posed diffuser inlet condition, the mixing plane location was thus set to 20% of the impeller exit width downstream of the impeller exit where the mixed out flow field does not contain reverse flow. Figure 2-7 shows the resulting radial velocity profile.

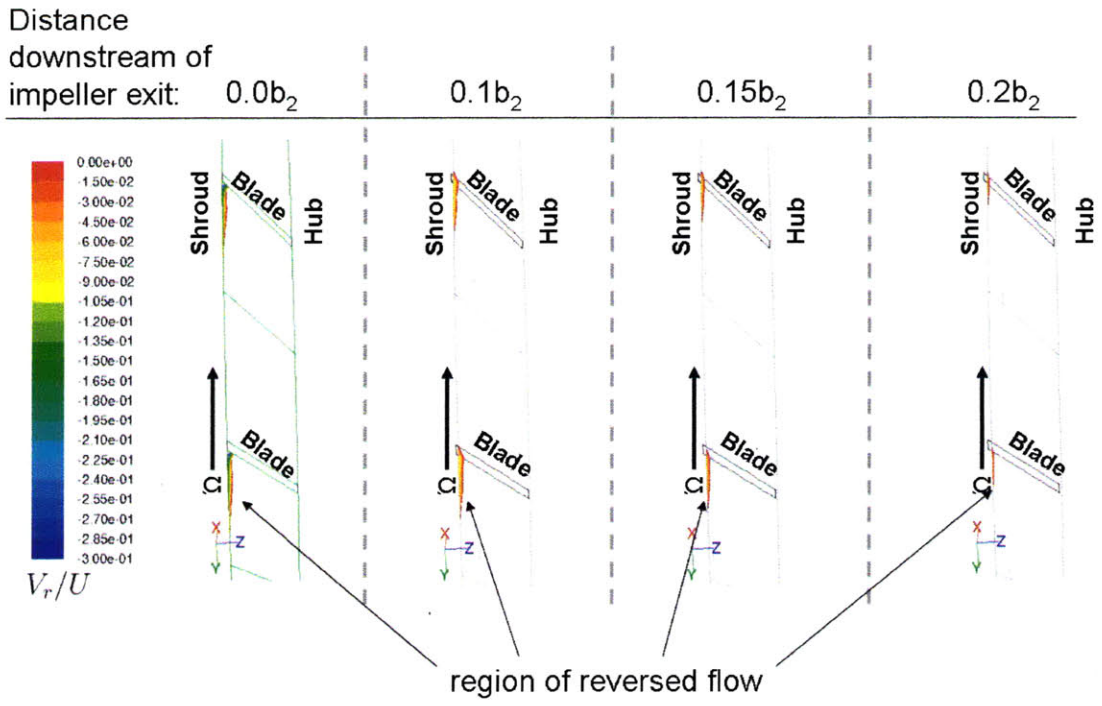

Figure 2-6: Contours of radial velocity at four radial stations near the impeller exit.

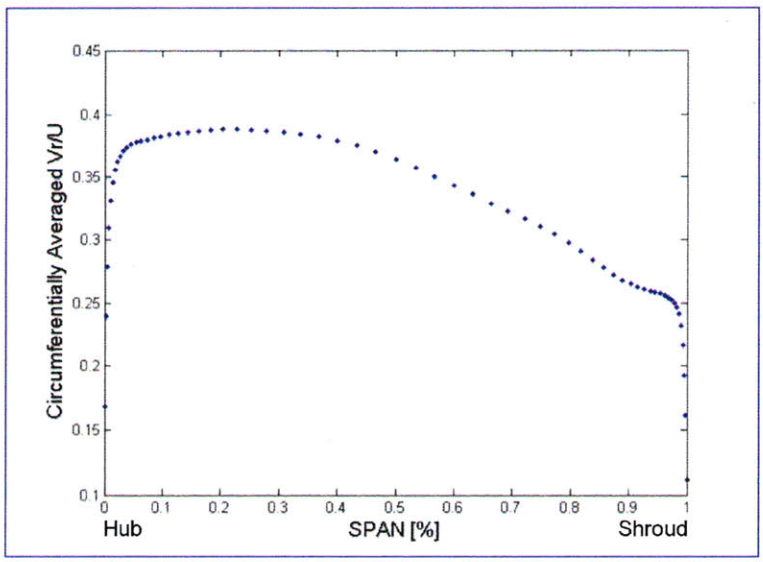

Figure 2-7: Radial velocity profile at mixing plane location.

Chapter 3

Baseline Return Passage Assessment

This section describes the features of flow in the baseline return passage. A combination of quantitative and qualitative tools was used, with the objective of identifying the loss mechanisms which can be mitigated or eliminated through design. The loss coefficient of each component was calculated separately to isolate the contribution of that component to the total return passage losses. Contours of velocity and entropy production rate were also used to help identify the loss mechanisms. While calculations were performed for the range of flow coefficients from $\Phi/\Phi_d = 0.89$ to $\Phi/\Phi_d = 1.17$, only the flow field at the design condition, $\Phi/\Phi_d = 1$, was examined in depth.

3.1 Flow Features and Loss Mechanisms in the Baseline Return Passage

Figure 3-1 is a plot of component loss coefficients as a function of flow coefficient from $\Phi/\Phi_d = 0.89$ to $\Phi/\Phi_d = 1.17$. At $\Phi/\Phi_d = 1$ the loss coefficients of the diffuser, return bend and return vane components are approximately 0.05. The loss coefficient of the 90° bend is about one third of this value.

The losses in the diffuser might be expected to be higher than losses in the return bend and return vane because the velocity in the diffuser is higher and thus the

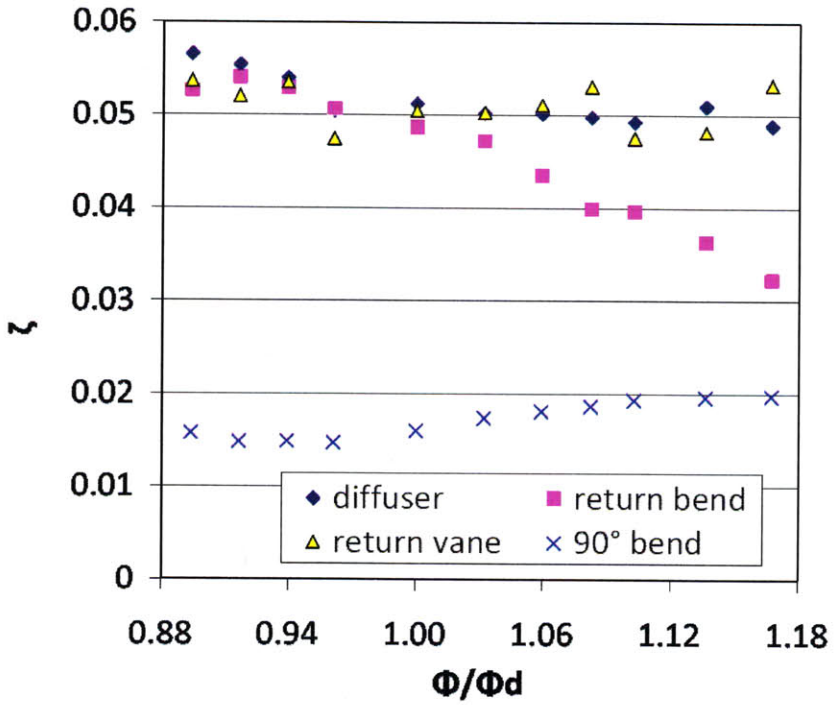

Figure 3-1: Component loss coefficients in the baseline return passage.

entropy production per unit area due to boundary layer dissipation, which scales with the cube of the local velocity, is higher. High losses in the return bend and return vane, despite lower kinetic energy relative to the diffuser, indicate a potential for improvement in these components. Detailed assessment of the baseline return passage flow thus focused on the return bend and return vane.

Increases and decreases of static pressure rise indicate deceleration and acceleration of the flow, respectively. Figure 3-2 shows the circumferentially area-averaged values of static pressure rise on the hub and shroud surface as a function of distance through the diffuser, return bend and return passages. The static pressure rise coefficient is defined as:

$$Pressure\ Rise\ Coefficient = \frac{P - P_2}{1/2\rho_2 V_2^2}. \tag{3.1}$$

The figure shows that about 80% of the pressure rise in the return passage occurs in the diffuser. Streamline curvature in the return bend implies a spanwise pressure

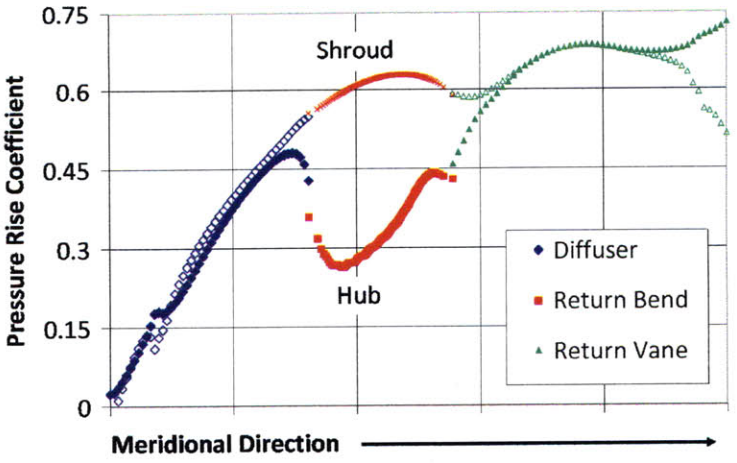

Figure 3-2: Pressure rise coefficient in the baseline return passage.

gradient, with higher pressure on the concave shroud surface and lower pressure on the convex hub surface. The spanwise pressure gradient results in acceleration on the hub, seen in Figure 3-2 as a drop in pressure rise coefficient in the last 10% of the diffuser and first 25% of the return bend. The acceleration is followed by deceleration on the hub in the latter half of the return bend as it transitions to the straight return vane section. The adverse pressure gradient on the hub causes the flow to separate at the exit of the return bend. The pattern of acceleration and deceleration on the hub in the bend is unavoidable because of the turning in the return bend, but, as will be shown in section 4.1.1, the magnitude and location of the adverse pressure gradient peak can be modified.

On the shroud the pressure rise continues until midway through the return bend where the flow accelerates into the return vane. The acceleration is seen in Figure 3-2 as a drop in the shroud pressure rise coefficient at the exit of the return bend and the inlet of the return vane. The return vane removes the swirl component of velocity, but only 6% of the stage pressure rise is achieved in the return vane passage because the flow area is reduced at the smaller radius. At the exit of the return vane the static pressure on the shroud decreases and the static pressure on the hub increases due to the meridional streamline curvature in the 90° bend.

A more detailed description of the flow field and loss mechanisms in each compo-

nent is provided below.

3.1.1 Diffuser Flow Features

Figures 3-3 and 3-4 show contours of the velocity magnitude and entropy production in the diffuser. The losses are dominated by viscous dissipation in the boundary layer, with no appreciable secondary flow structures which contribute in a substantive manner. As such, improved diffuser performance can only be achieved by increasing the diffuser width ratio to decrease the velocity and reduce boundary layer losses, and MHI has shown that diffuser performance can improve with increases in diffuser exit width[1].

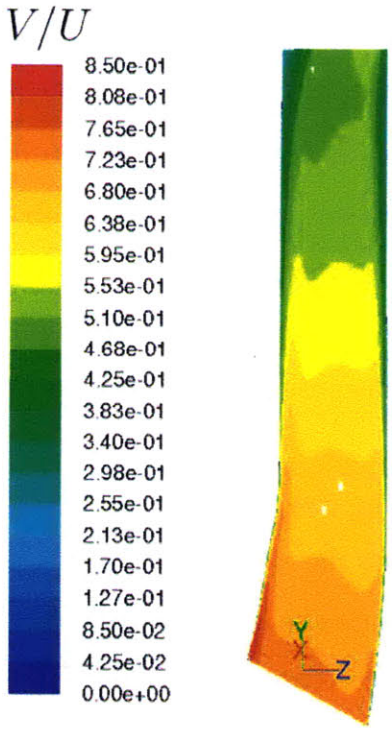

Figure 3-3: Contours of velocity magnitude in the baseline diffuser.

[1]Personal communication from MHI

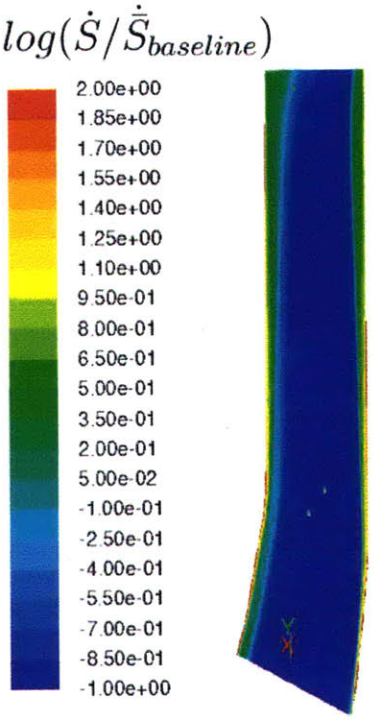

Figure 3-4: Contours of $log(\dot{S}/\dot{\bar{S}}_{baseline})$ in the baseline diffuser.

3.1.2 Return Bend Flow Features

Figure 3-5 shows contours of velocity magnitude in the return bend. Acceleration and subsequent deceleration of the flow on the hub in the return bend can be seen, with peak velocity on the hub occuring around 25% through the bend. Acceleration into the bend corresponds to a trough in pressure gradient at the inlet of the return bend, which is seen in the plot of pressure gradient, $\frac{dP/dl}{(1/2\rho V^2)_2/b_2}$, as a function of distance through the diffuser and return bend, Figure 3-6. The adverse pressure gradient associated with deceleration in the latter 75% of the return bend is also seen. The adverse pressure gradient increases through the return bend with a peak value near the return bend exit where separation begins.

The separation in Figure 3-5 is a region of low velocity magnitude near the hub surface at the exit of the return bend. Figure 3-7 shows contours of entropy production rate in the return bend. There is a region of high loss where separation begins.

On the return bend shroud there is a region of reversed flow which extends from

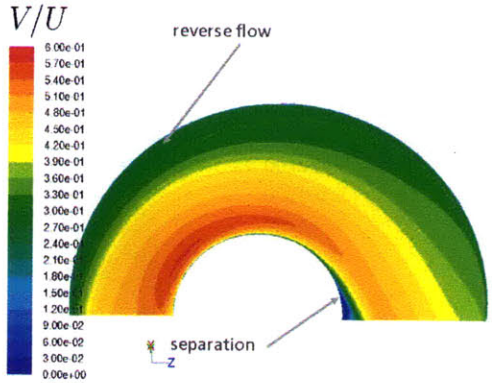

Figure 3-5: Contours of velocity magnitude in baseline return bend.

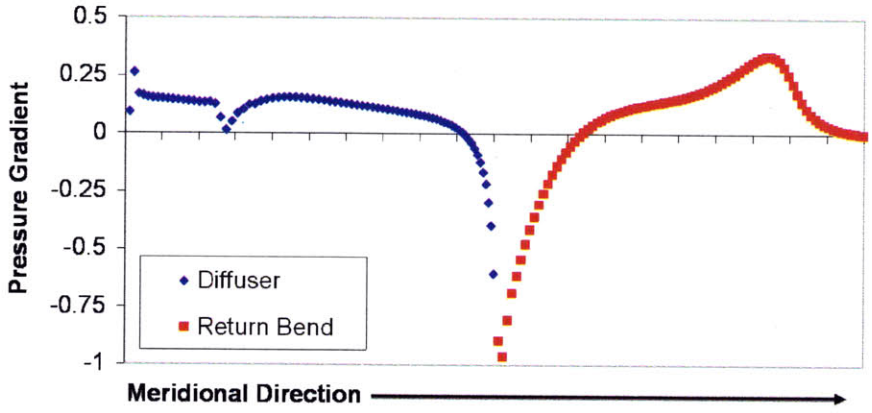

Figure 3-6: Pressure gradient on the hub surface through the baseline diffuser and return bend.

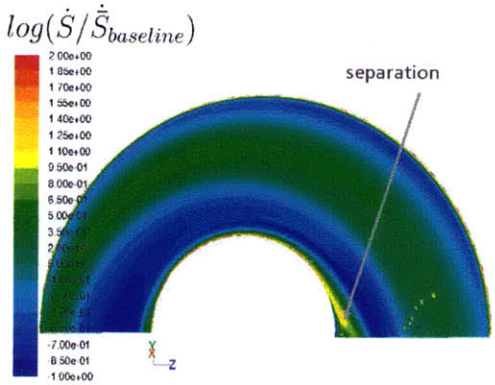

Figure 3-7: Contours of $log(\dot{S}/\bar{\dot{S}}_{baseline})$ in the baseline return bend.

the exit of the diffuser through roughly 60% of the bend. Apart from the isolated region of high loss associated with the flow separation at the bend exit and losses at the vane leading edge (described in section 3.1.3), the entropy produced in the return bend is due to dissipation in the boundary layer. The blockage associated with the reverse flow on the shroud increases the freestream velocity and the associated entropy production per unit area, and the non-zero leading edge incidence angle causes increased acceleration around the leading edge.

3.1.3 Return Vane Flow Features

Figures 3-8 and 3-9 show contours of radial velocity and entropy production rate at six radial stations along the return vane. The radial stations are arranged at intervals of 20% chord, from the 0% chord station at the leading edge to the 100% chord station at the trailing edge. The region of separation initiating in the return bend, which is indicated by red and orange in 3-8, extends across the entire pitch on the hub, with the highest reverse flow on the pressure side of the vane. Between the 0% and 20% chord stations the region of separation increases in size. The flow reattaches by the 40% chord station but a region of reduced velocity flow extends across the channel on the vane suction side. The reduced velocity region is present on the suction side through the remainder of the return vane.

A region of high loss from mixing of passage secondary flow is seen in Figure 3-9. This region of high loss extends into the passage on the vane suction side between the 20% and 60% chord stations. Blockage from the low velocity flow also increases the local velocity and hence the entropy production per unit area in the return vane.

Figure 3-10 shows the incidence angle at the leading edge radial station as a function of span. Flow at the vane leading edge exhibits positive incidence angles between 50% and 100% of the span, with incidence angles up to 15.5° at the shroud. The positive incidence angle at the hub is due to separation. Positive incidence contributes to the losses in the return vane and near the exit of the return bend.

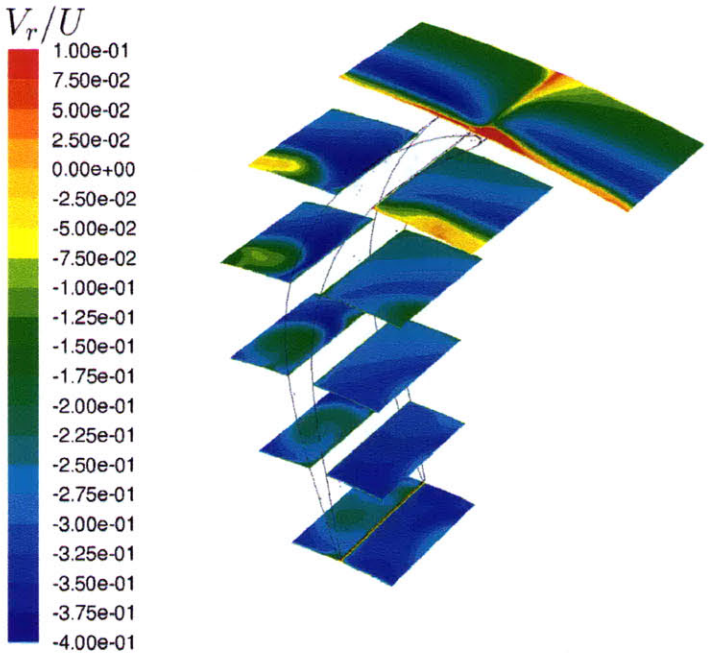

Figure 3-8: Contours of radial velocity on passage cross sections in the baseline return vane.

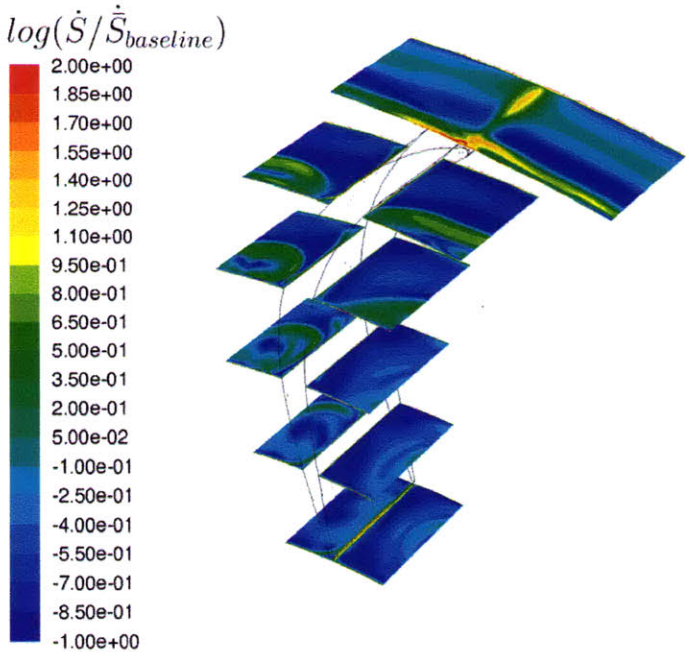

Figure 3-9: Contours of $log(\dot{S}/\bar{\dot{S}}_{baseline})$ on passage cross sections in the baseline return vane.

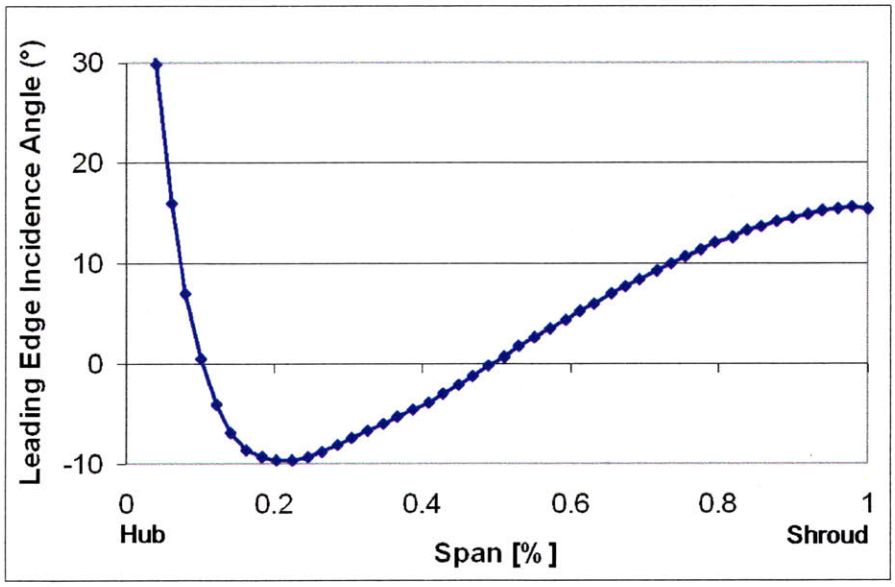

Figure 3-10: Incidence angle at the baseline return vane leading edge.

Chapter 4

Development of New Return Passage Concept

This section describes the development of improved return passage concepts. The design process was described in section 2.1, and encompasses steps 4-6 in the technical approach, as given below:

Technical Approach

4. Define Design Objective (based on flow features of previous return passages)

5. Screen Design Concepts

   - Define meridional geometry of preliminary concepts.
   - Perform axisymmetric calculation of preliminary concepts to determine impact.

6. Three-dimensional Calculation of Candidate Return Passage

   - Define meridional geometry of candidate concept.
   - Perform axisymmetric calculations to verify candidate design addresses design objective.

- Define three-dimensional geometry using flow angle from axisymmetric calculation to define return vane leading edge lean angle (in conjunction with Dr. M.V. Casey[1]).
- Perform three-dimensional calculation of candidate design and perform detailed assessment of flow field.

The initial design objective was to address separation at the exit of the return bend in the baseline return passage, but this objective was modified to incorporate improvement of the diffuser and return bend performance, based on assessment of the flow in the candidate return passage. The screening and development of candidate concepts is described in this section.

4.1 Screening of Preliminary Concepts

4.1.1 Design Concepts to Eliminate Separation at Bend Exit

In section 3.1 separation on the hub at the exit of the return bend in the baseline return passage was shown to be an important source of loss in the return bend and return vane. The initial objective for the redesigned return passage was to eliminate the region of separation at the return bend exit. To this end, the effect of meridional geometry modifications on separation was considered, including increased diffuser exit width. Axisymmetric calculations of the flow field in several alternative geometries were performed. The modifications which were studied are:

- Increasing diffuser width
- Decreasing return bend channel width
- Increased axial extent of return bend
- Non-constant curvature in return bend

[1]Dr. M. V. Casey defined the return vane leading edge lean angle and blade airfoil coordinates.

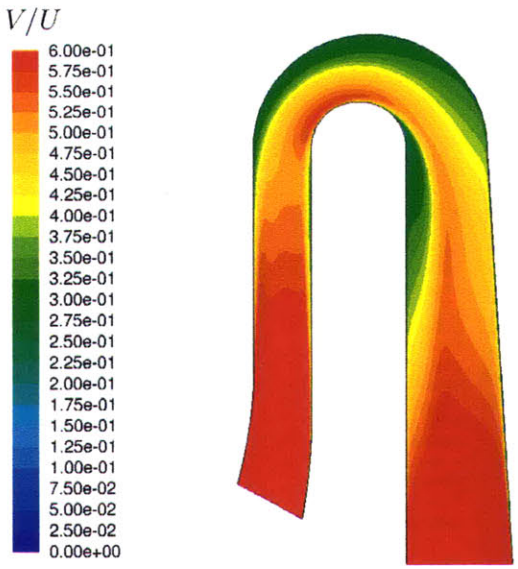

Figure 4-1: Contours of velocity magnitude from an axisymmetric calculation of the baseline return passage flow.

Each concept is described below, along with its merits and demerits. All of the designs maintain the location and width of the diffuser inlet and return vane trailing edge station from the baseline return passage. For reference, contours of velocity magnitude for the baseline geometry, from an axisymmetric calculation, is provided in Figure 4-1:

- **Preliminary Design PD-A** is similar to the baseline return passage but has a 25% wider diffuser exit. The hub wall contour and return bend exit width are kept the same. Figure 4-2 shows contours of velocity magnitude in PD-A, with the baseline meridional geometry overlaid. There is a region of separation at the exit of the return bend similar in size to the separation region in the baseline return passage, which implies the increased diffuser width does not reduce separation at the return bend exit. The magnitude of the peak velocity near the hub in the return bend is lower than baseline, which is consistent with a 0.02 points higher pressure rise at the diffuser exit in PD-A compared with the baseline.

  Figure 4-3 gives the total entropy generated in a vaneless, radial diffuser with

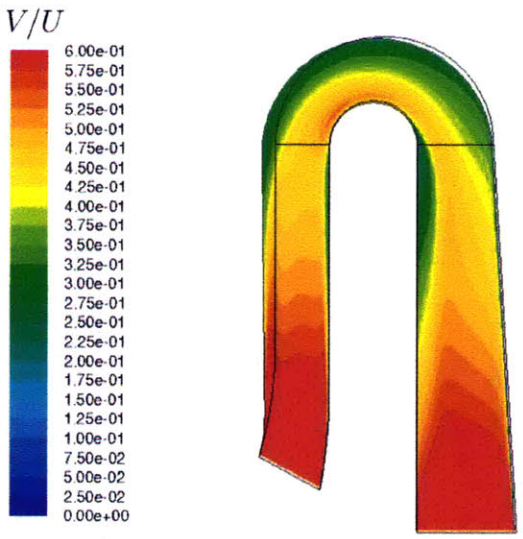

Figure 4-2: Contours of velocity magnitude from an axisymmetric calculation of flow in PD-A overlaid on baseline geometry.

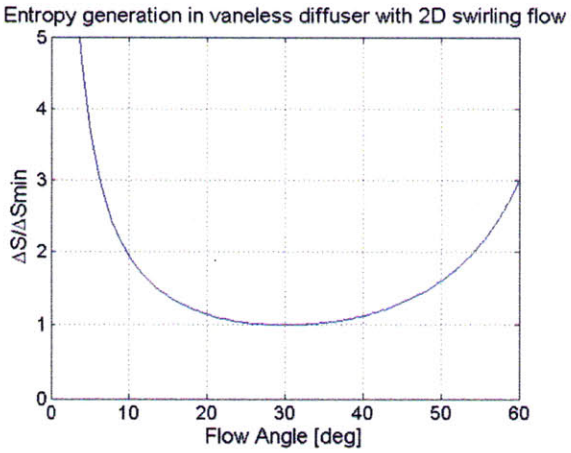

Figure 4-3: Change in entropy as a function of flow angle in a vaneless, two-dimensional radial diffuser.

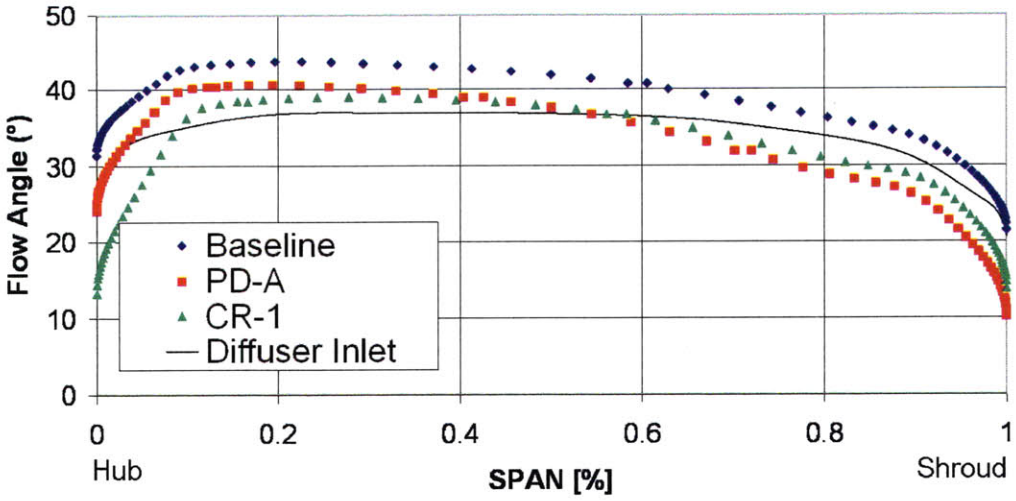

Figure 4-4: Flow angle across the span midway through the diffuser of selected geometries.

fixed mass flow and two-dimensional swirling flow, as a function of flow angle. In the figure ΔS is the change in entropy flux between the outlet and the inlet, not the volumetric entropy production rate. Minimum entropy change, ΔS_{min}, occurs at a flow angle of roughly 30° from tangential, though flow angles up to 35° are useful to avoid separation on the shroud[2]. Figure 4-4 shows flow angle profiles midway through the diffuser, from axisymmetric calculations. The flow angle in PD-A is in the range of 30-40°.

- **Preliminary Design PD-B** maintains the baseline geometry from inlet to midway through the return bend, at which point the channel width is reduced to counter flow deceleration on the hub in the return bend. Reducing channel width eliminates separation at the return bend exit, as seen in Figure 4-5, which shows contours of velocity magnitude. The constriction in PD-B results in increased flow velocity in the return bend which increases the losses from boundary layer dissipation; less constriction, or even a constant area bend, should help reduce separation compared with baseline.

[2]Personal communication with Dr. M. V. Casey.

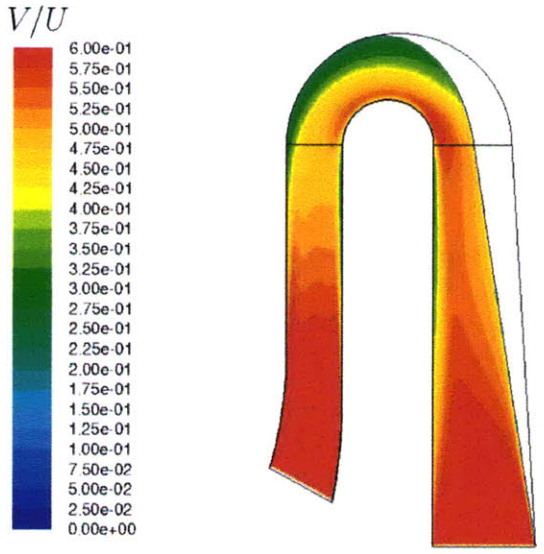

Figure 4-5: Contours of velocity magnitude from axisymmetric calculation of flow in PD-B overlaid on baseline geometry.

- In **Preliminary Design PD-C** the axial extent of the return bend is increased by angling the outer portion of the return vane towards the downstream stage. Figure 4-6 shows contours of velocity magnitude for PD-C. The geometry is also overlaid on the baseline geometry, and it can be seen that PD-C has a radial shroud wall and angled hub wall, as opposed to a radial hub wall and angled shroud wall in the baseline geometry. The increased axial extent of the bend is combined with decreasing curvature through the bend. The radius of curvature at the bend inlet is equal to the baseline bend radius and increases in the downstream portion of the bend. The size of the separation region is reduced compared with the baseline, indicating that the increased axial extent has addressed the separation at the exit of the return bend.

- **Preliminary Design PD-D** employs a curved 'S' diffuser to sweep the diffuser towards the upstream stage and increase the axial extent of the return bend beyond that in PD-C. The increased axial extent is combined with increasing curvature through the bend. The radius of curvature at the bend inlet is larger than the baseline bend radius and decreases to the baseline radius at

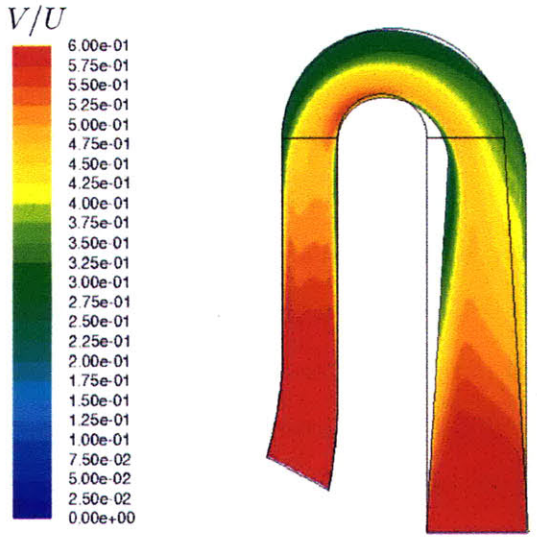

Figure 4-6: Contours of velocity magnitude from an axisymmetric calculation of flow in PD-C overlaid on baseline geometry.

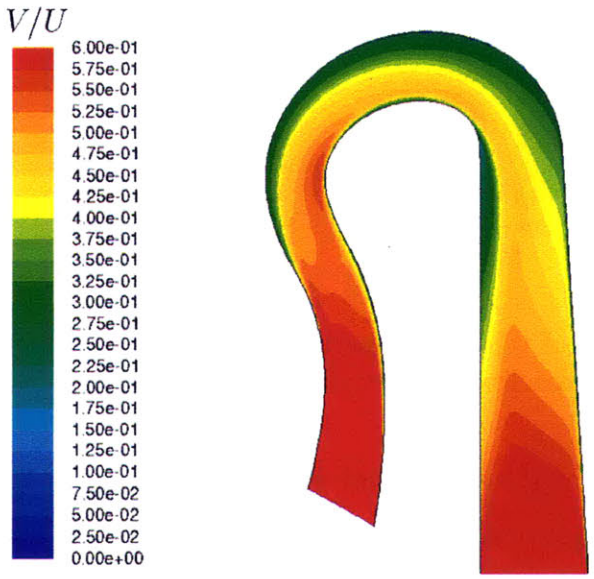

Figure 4-7: Contours of velocity magnitude from an axisymmetric calculation of preliminary design PD-D overlaid on baseline geometry.

the bend exit. Figure 4-7 shows contours of velocity magnitude in PD-D and the separation region is seen to be smaller than in the baseline case, but larger than that in PD-C.

- **Preliminary Design PD-E** also employs a curved 'S' diffuser to increase the axial extent of the return bend to that of PD-D. The increased axial extent of the bend is combined with decreasing curvature through the bend, qualitatively similar to PD-C. In Figure 4-8, which shows contours of velocity magnitude in PD-D, there is no separation at the return bend exit, implying the combination of increased axial extent and decreasing curvature through the bend is effective in eliminating separation at the bend exit.

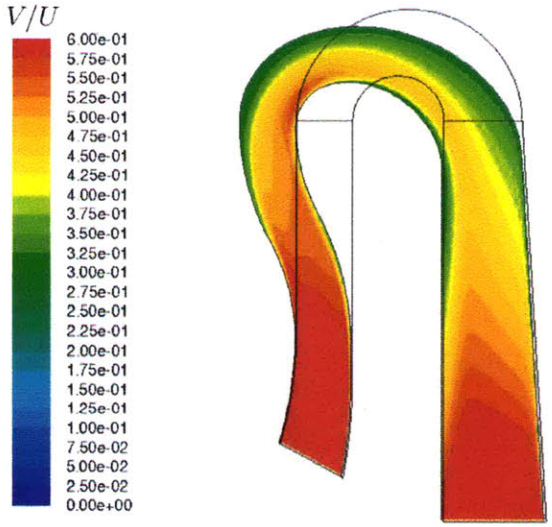

Figure 4-8: Contours of velocity magnitude from an axisymmetric calculation of flow in PD-E overlaid on baseline geometry.

A comparison of the meridional pressure gradient, $\frac{dP/dl}{(1/2\rho V^2)_2/b_2}$, on the hub for PD-E, CR-1 (described later) and baseline as a function of meridional length is presented in Figure 4-9. The figure shows PD-E peak adverse pressure gradient is shifted upstream compared with the baseline, occuring near 25% through the bend, immediately downstream of the maximum acceleration. The upstream shift in peak adverse pressure gradient results in pressure recovery after the

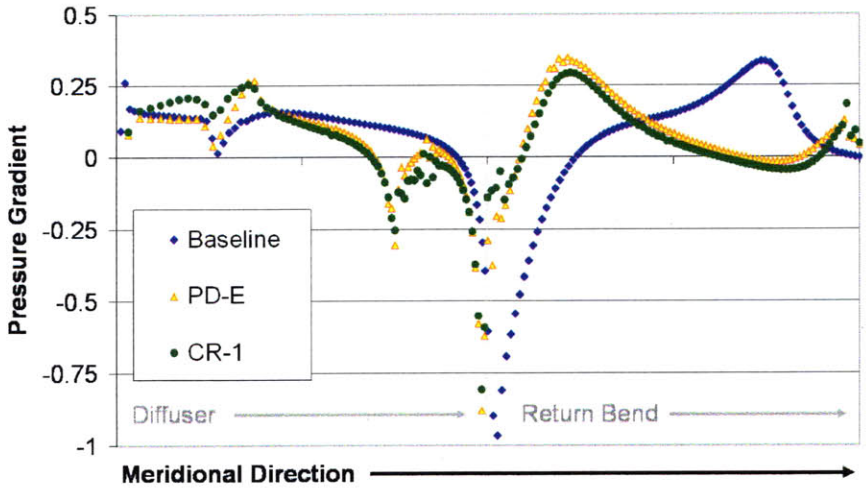

Figure 4-9: Pressure gradient in the baseline, PD-E and CR-1 diffuser and return bends.

acceleration on the bend rather than further downstream in the return bend. The peak adverse pressure gradient occurs where the boundary layer is thin because of the acceleration into the bend, as seen in velocity contours near the return bend, Figure 4-10. The adverse pressure gradient then decreases through the bend, reducing the local loading in the downstream portions of the bend where the boundary layer is thick and the flow more likely to separate.

4.1.2 Candidate Return Passage 1 (CR-1)

The meridional geometry of candidate return passage 1 (CR-1) incorporates a number of design features present in one or more of the preliminary designs. Specifically, the 'S' diffuser is combined with a return vane which is angled towards the downstream stage to allow an axial extent greater than both PD-E and PD-C. The decreasing curvature through the bend, present in PD-E and PD-C, is present in CR-1. While not as severe as the constriction in PD-B, CR-1 employs a constant area bend rather than the increasing area bend used in the baseline. To reduce losses in the diffuser, the diffuser exit width is increased from baseline.

Figure 4-11 shows contours of velocity magnitude in CR-1. There is no separation

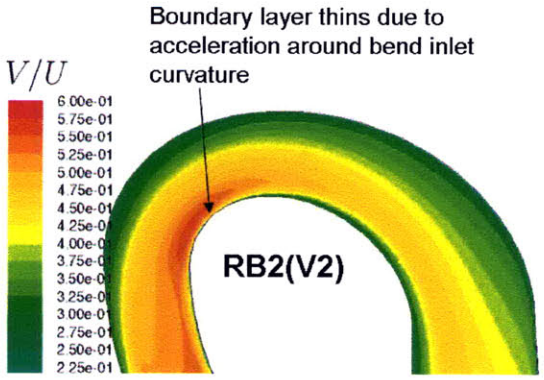

Figure 4-10: Contours of velocity magnitude near the PD-E return bend from an axisymmetric calculation.

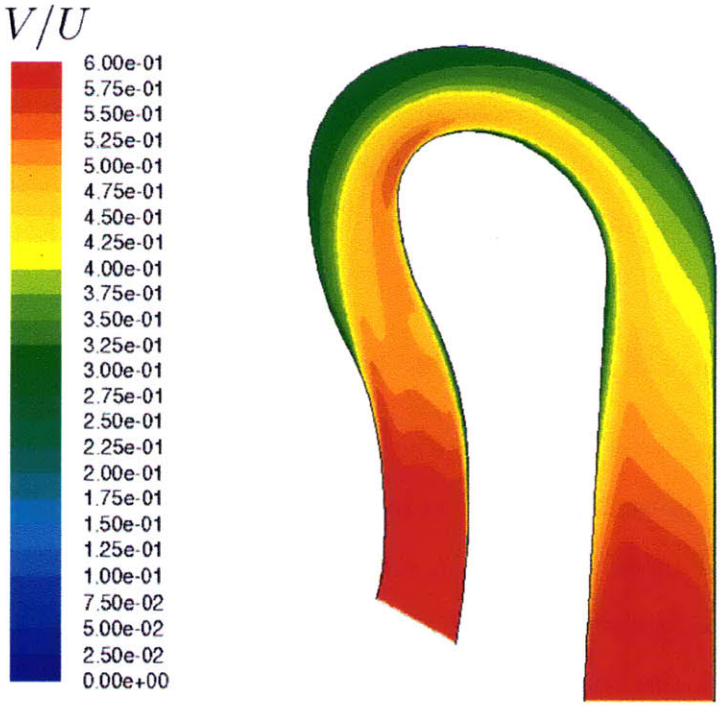

Figure 4-11: Contours of velocity magnitude in CR-1 from an axisymmetric calculation.

at the exit of the bend. As with PD-E, the peak adverse pressure gradient, is shifted upstream of the baseline, and is reduced in magnitude due to the constant area bend.

To ensure CR-1 was suitable in off-design conditions calculations were performed at flow coefficients $\Phi/\Phi d = 0.89$ and $\Phi/\Phi d = 1.17$. Contours of velocity magnitude at these off-design conditions are presented in Figure 4-12. The flow remains attached at the return bend exit in both cases.

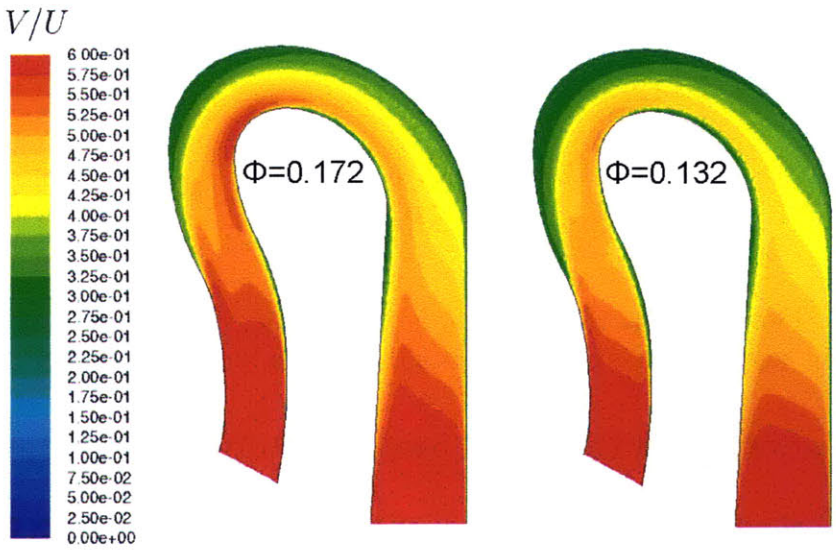

Figure 4-12: Contours of velocity magnitude in CR-1 from axisymmetric calculations at $\Phi/\Phi_d = 0.89$ and $\Phi/\Phi_d = 1.17$.

In section 3.1.3 the incidence angle mismatch at the return vane leading edge contributed to loss in the baseline return vane and return bend. To better match the return vane to the flow, the leading edge lean angle for the three-dimensional CR-1 geometry was based on the flow angle at the leading edge radial station. Due to limited geometry creation capabilities a linear variation in lean angle was selected .

The flow angle profile versus span at the leading edge radial station for the CR-1 and baseline return passages is given in Figure 4-13. The metal angle profile is shown as a dashed line from 40° at the hub to 20° at the shroud. It should also be noted that the attached flow in CR-1 has a hub angle of 30°, compared with the negative flow angle on the hub in the baseline design.

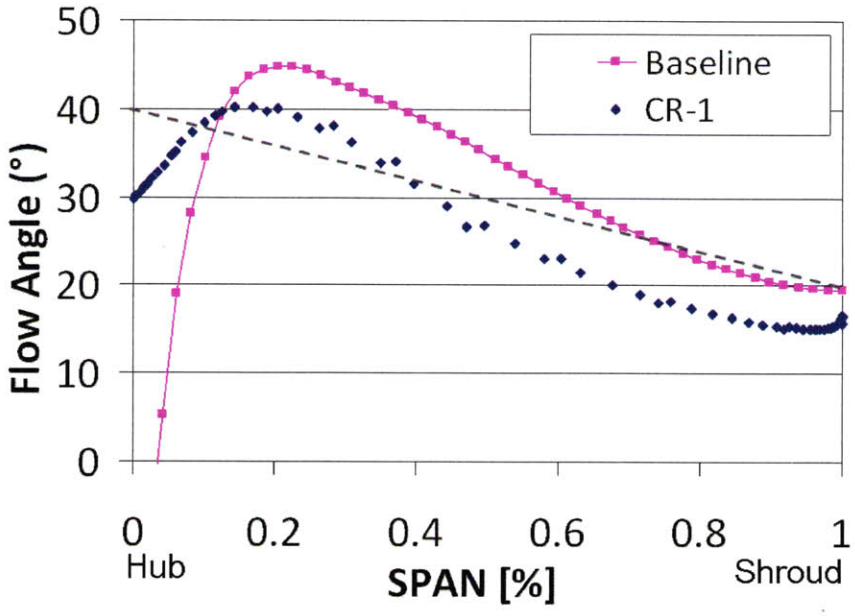

Figure 4-13: Flow angle at the return vane leading edge for baseline and CR-1. The CR-1 leading edge metal angle profile is indicated as a dashed line.

4.1.3 Concepts to Reduce Losses in Diffuser and Return Bend

A second iteration focused on reducing losses in the diffuser and return bend. As will be discussed in section 4.2.1, the convex curvature on the shroud in the 'S' diffuser led to flow reversal midway through the diffuser and the increased blockage associated with separation caused an increase in entropy production per unit area in the diffuser. The initial CR-1 concept did not address the boundary layer dissipation losses in the return bend.

The objective of the preliminary concepts presented in this section is to maintain the attached flow on the hub at the return bend exit while reducing the losses in the diffuser and return bend relative to CR-1. The design modifications considered are:

- Straight or partially straight diffuser walls
- Radial location and radius of curvature of diffuser "bend"
- "Pinch" at diffuser exit

The geometries examined are described below. All of these exhibit increased axial

extent, compared with baseline, and decreasing curvature in the return bend.

- **Preliminary Design PD-F** employs sharp convex curvature near the diffuser inlet to turn the diffuser towards the upstream stage. Straight walls sweep left to increase the axial extent of the return bend. To implement decreasing curvature through the entire bend with this type of swept diffuser requires a smaller radius of curvature at the bend inlet than the baseline return bend radius of curvature. Contours of velocity magnitude for PD-F are shown in Figure 4-14.

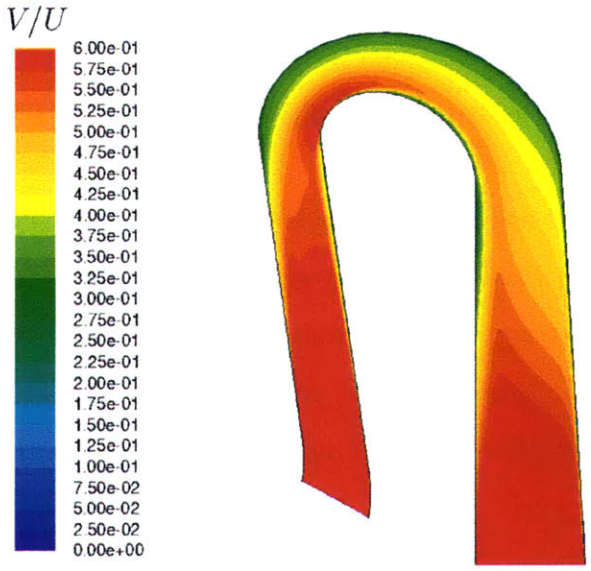

Figure 4-14: Contours of velocity magnitude in PD-F from axisymmetric calculations.

Figure 4-15 shows the pressure rise through the diffuser of PD-F and of the baseline return passage, plotted against l, the non-dimensional meridional length. The pressure rise for the PD-F diffuser is lower than baseline on both the hub and shroud surfaces. This is likely due to the blockage associated with a region of reverse flow on the shroud beginning at the sharp convex curvature at diffuser inlet and extending through the return bend. Figure 4-14 also indicates a large area of high velocity flow (red) on the hub at the return bend inlet, and the peak velocity in the return bend is 11.1% higher than baseline, leading to increased entropy production per unit area in the return bend.

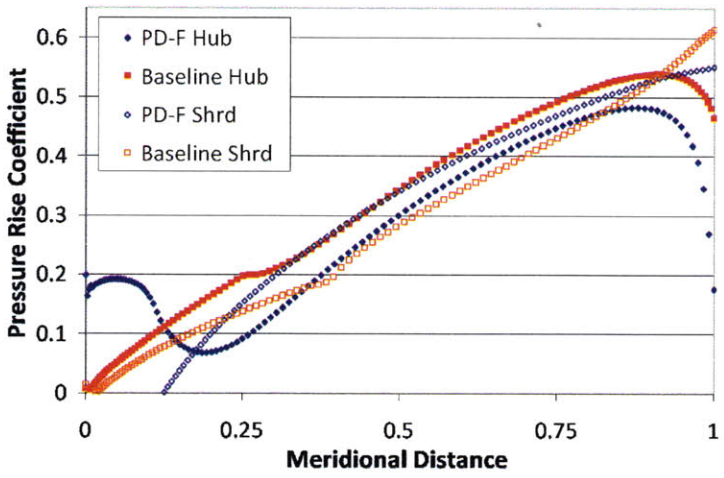

Figure 4-15: Pressure rise coefficient through the PD-F diffuser.

- **Preliminary Design PD-G** avoids the sharp convex curvature of PD-F. PD-G maintains the baseline diffuser geometry through the mid-diffuser "pinch", at which point straight diffuser walls sweep left to increase the axial extent of the return bend. Like PD-F, the radius of curvature at the inlet of the PD-G return bend is smaller than the radius of curvature at the inlet of the baseline return passage.

  Figure 4-16 shows the PD-G meridional geometry and contours of velocity magnitude.Streamline curvature in the diffuser implies a spanwise pressure gradient, with higher pressure on the concave shroud surface in the outer portion of the diffuser. The high pressure rise on the shroud surface (due to the curvature) leads to separation, which begins about 80% through the diffuser on the shroud wall. The separation is seen as a region of negative flow angle in Figure 4-17, which shows contours of flow angle in the PD-G diffuser. Nevertheless, losses in the PD-G diffuser are lower than in the PD-F diffuser, which is consistent with the higher diffuser pressure rise in PD-G (relative to PD-F) seen in the plot of pressure rise coefficient versus meridional length through the diffuser in Figure 4-18. The region of high velocity flow on the hub is also smaller than in PD-F, with a peak return bend velocity 5.6% higher than baseline. The pressure rise in the diffuser is lower than that of baseline on the hub and shroud surfaces,

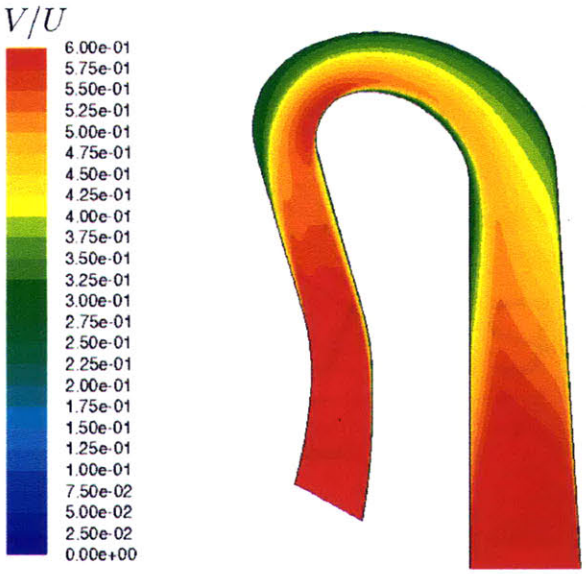

Figure 4-16: Contours of velocity magnitude from an axisymmetric calculation of flow in PD-G.

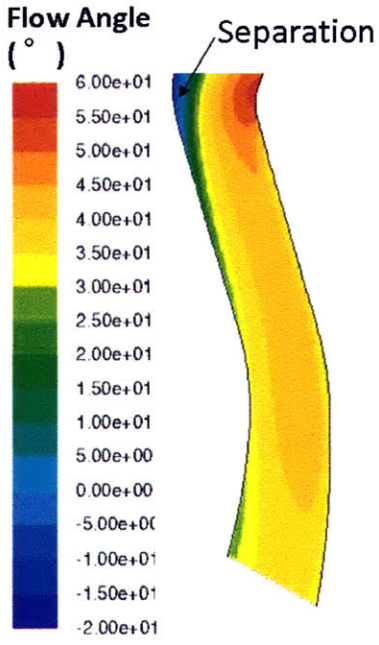

Figure 4-17: Contours of diffuser flow angle from an axisymmetric calculation of flow in PD-G.

which indicates the performance of the PD-G diffuser is worse than the baseline diffuser.

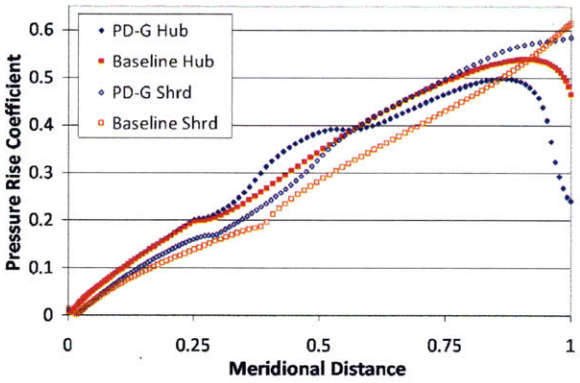

Figure 4-18: Pressure rise coefficient through the PD-G diffuser.

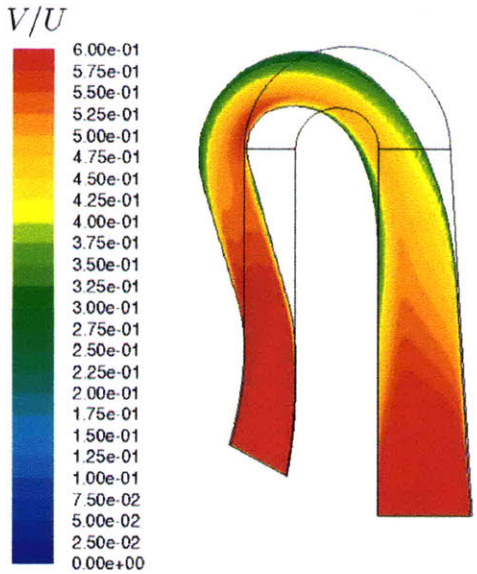

Figure 4-19: Contours of velocity magnitude from axisymmetric calculations of flow in PD-H

- **Preliminary Design PD-H** is similar to PD-G but the diffuser exit is "pinched" by 8% to avert separation on the shroud near the diffuser exit and in the return bend. To avoid sharp curvature at the entrance to the return bend, a constant radius of curvature is employed on the first quarter of the shroud and first half of the hub, where the flow accelerates. The constant radius portion is followed

by an increasing radius of curvature in the remainder of the return bend. Figure 4-19 shows the PD-H meridional geometry and contours of velocity magnitude. The flow is fully attached in the diffuser and return bend. The "pinch" and constant curvature at the return bend inlet eliminate the reverse flow on the shroud in both the diffuser and the return bend. The reduced blockage creates a higher pressure rise in the diffuser than PD-F and PD-G. The pressure rise through the diffuser on the shroud surface, shown in Figure 4-20 as a function of meridional distance, is equal to that of the baseline return passage. The region of high velocity flow on the hub in the return bend is smaller than in PD-F and PD-G and the peak velocity is only 0.7% higher than baseline.

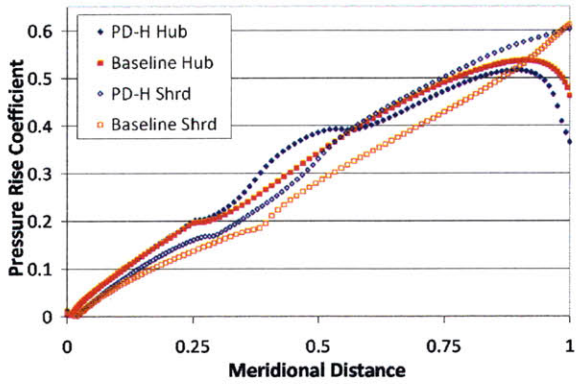

Figure 4-20: Pressure rise coefficient through the PD-H diffuser.

The change in loss coefficient for each preliminary concept, relative to the baseline value, is summarized in Table 4.1. Comparisons are made at 75% and 100% through the diffuser and at the return bend exit (100% bend). In PD-F and PD-G a large increase in loss is seen in the portions of the diffuser which have reverse flow, i.e., the final 25% for PD-G and the entire diffuser for PD-F. PD-H has higher losses in the diffuser compared with baseline, but exhibits a net improvement through the return bend.

Table 4.1: Change in loss coefficient from baseline.

Station	PD-F	PD-G	PD-H
75% Diffuser	11.9%	3.8%	0.3%
100% Diffuser	21.8%	16.0%	0.7%
100% Bend	14.1%	2.7%	-7.9%

4.1.4 Candidate Return Passage 2 (CR-2)

The improvements found for the PD-H geometry were promising enough that this geometry was used as the baseline for candidate return passage 2 (CR-2). As with CR-1, the leading edge lean angle was selected to match the flow angle given by the axisymmetric calculation. Figure 4-21 shows the calculated flow angle, as a function of distance across the span, at the leading edge radial station for CR-2 and the for baseline return passage. The leading edge metal angle for CR-2 is shown as a dashed line from 38° on the hub to 22° on the shroud.

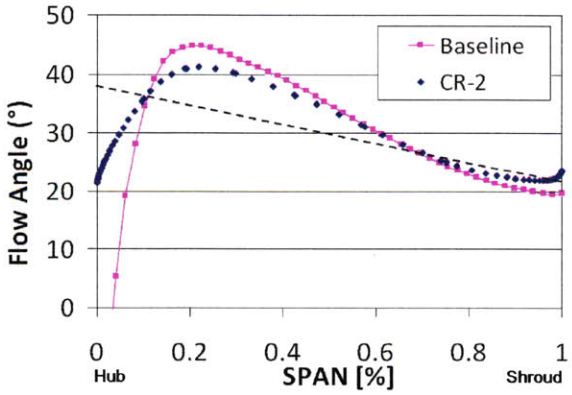

Figure 4-21: Flow angle at the return vane leading edge for baseline and CR-2. The CR-2 leading edge metal angle profile is indicated as a dashed line.

4.1.4.1 Sensitivity to changes in diffuser inlet flow angle

To ensure CR-2 would be suitable over a range of inlet flow angles and flow coefficients, the sensitivity of the diffuser and bend losses and flow to changes in inlet conditions

was studied. Five cases were considered. Diffuser inlet flow profiles and mass flow from the Φ/Φd=0.89, the design flow, and Φ/Φd=1.17 calculations of the baseline impeller were used. The flow angle on the shroud was also modified by plus and minus five degrees from the design flow profile while maintaining the design mass flow. The latter two cases are denoted "shroud minus 5°" and "shroud plus 5°". The five diffuser inlet flow angle profiles used in the sensitivity study are shown in Figure 4-22.

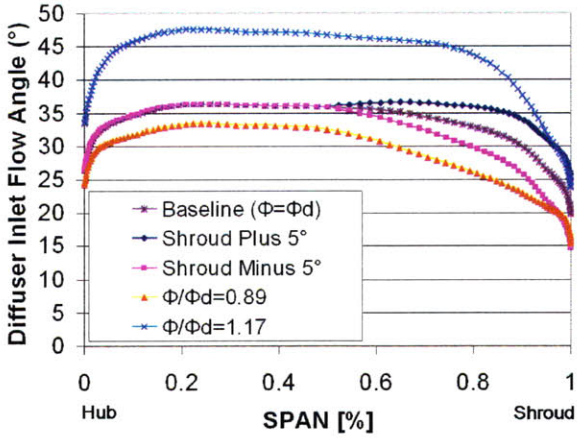

Figure 4-22: Flow angle profiles at the diffuser inlet.

The performance trends through the return bend are similar for the four off-design boundary conditions considered. Table 4.2 gives the change in loss coefficient between CR-2 and the baseline at three flow stations for the five flow conditions described above. For all conditions except Φ/Φd=0.89, the CR-2 loss coefficient is 0.1-2.9% higher than baseline through the diffuser. For Φ/Φd=0.89 the loss coefficient is 0.5% lower than baseline. For all conditions, the cumulative loss coefficient through the CR-2 return bend is 5.0-7.9% lower than baseline.

The flow in CR-2 is fully attached in the diffuser and return bend for all five

Table 4.2: Change in loss coefficient between CR-2 and baseline for five flow conditions.

Station	$\Phi/\Phi_d = 0.89$	$\Phi/\Phi_d = 1.0$	$\Phi/\Phi_d = 1.17$	-5°	+5°
75% Diffuser	0.1%	0.3%	0.7%	-0.2%	0.8%
100% Diffuser	-0.5%	0.7%	2.9%	0.1%	1.3%
100% Bend	-6.4%	-7.9%	-5.0%	-7.7%	-6.8%

conditions described above. Contours of flow angle for the $\Phi/\Phi_d = 0.89$ and "shroud minus 5°" cases, which have lower flow angle near the shroud than the other three cases, are shown in Figure 4-23.

In the following sections, results from three-dimensional calculations of the CR-1 and CR-2 return passages are discussed.

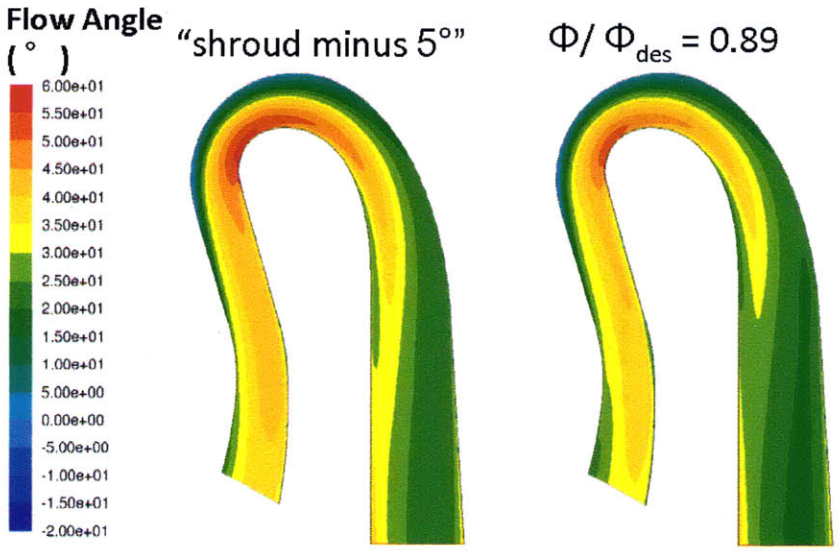

Figure 4-23: Contours of flow angle in CR-2 with $\Phi/\Phi_d = 0.89$ (left) and "shroud minus 5°" (right) inlet profiles.

4.2 Discussion of CR-1 Calculation Results

The cumulative loss coefficient in CR-1 is 2% higher than baseline. There is no separation at the exit of the return bend, and the losses in the return vane and 90° bend are reduced by 20% and 17%, respectively, compared to the basline. The losses in the diffuser are 31% higher than baseline. The losses in the return bend are the same as baseline. Individual component loss coefficients are summarized in Table 4.3.

Table 4.3: Change in loss coefficient from three-dimensional calculations of flow in CR-1 and baseline return passages.

Component	$\Delta\zeta$
Diffuser	$\uparrow$32%
Bend	No Change
Vane	$\downarrow$20%
90°	$\downarrow$17%
CUMULATIVE	$\uparrow$2%

4.2.1 Flow Features and Loss Mechanisms in CR-1

The reduction of losses in the CR-1 return vane is due to lower mixing losses and less blockage associated with separation. The improved flow characteristics are a result of reducing the separation (which originated at the return bend exit in the baseline return passage), and reducing the incidence angle at the leading edge compared to the baseline. The latter is shown in Figure 4-24.

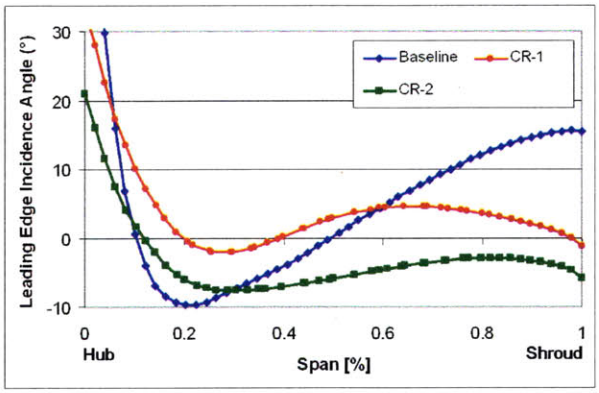

Figure 4-24: Incidence angle across the span at the return vane leading edge.

Figures 4-25 and 4-26 show contours of radial velocity and entropy production rate for the passage cross sections, respectively, at intervals of 20% chord through the return vane.

Comparison with the radial velocity in the baseline return vane (Figure 3-8) shows a smaller area of (red and orange) reverse flow at the leading edge radial station in CR-1. The reverse flow on the hub is confined to a small region near the vane and there is no reverse flow on the hub at the 20% chord station. A region of low velocity flow extends across the suction side of the vane from the 20% chord station through

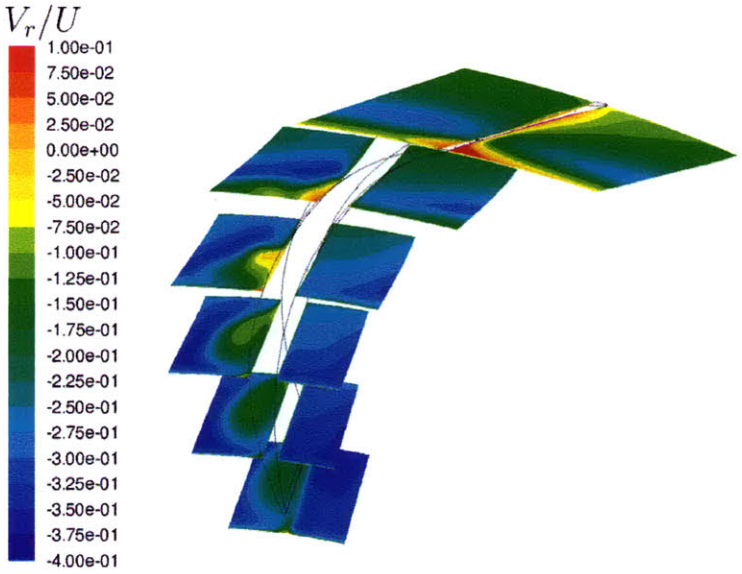

Figure 4-25: Contours of radial velocity on passage cross sections in the CR-1 return vane.

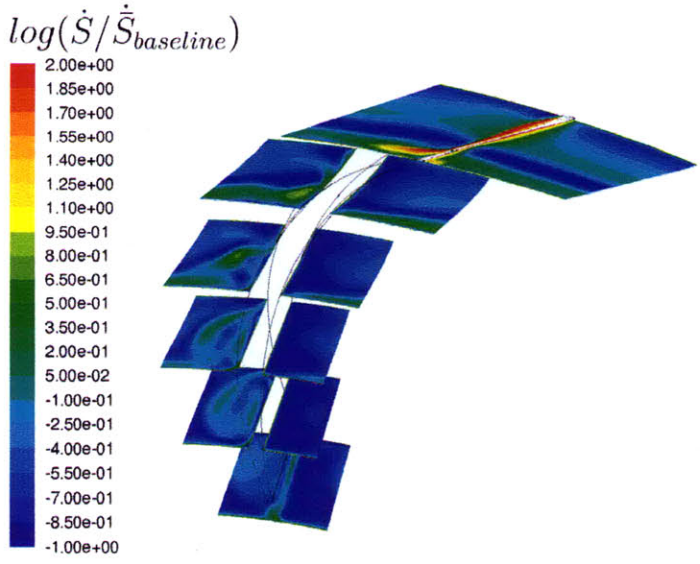

Figure 4-26: Contours of $log(\dot{S}/\dot{\bar{S}}_{baseline})$ on passage cross sections in the CR-1 return vane.

the 100% chord station. The reduced region of low velocity results in lower blockage and lower associated entropy production per unit wall area in the return vane. Figure 4-26 also shows a smaller region of entropy production from secondary flow mixing, which is localized on the suction side of the vane. Compare with the baseline return vane (see Figure 3-9).

There is a 31% increase in diffuser loss, resulting in a net increase in losses in CR-1 compared to the baseline. The increase in diffuser losses is the result of separation midway through the diffuser, where the convex curvature on the shroud turns to the left. Figure 4-27 shows contours of velocity magnitude in the diffuser and return bend. The vector plot in Figure 4-27 shows the separated region near the shroud wall in the outer half of the diffuser and the return bend. The blockage associated with separation increases the freestream velocity, increasing the boundary layer dissipation losses on the hub surface. The momentum flux at the diffuser exit is 5.5% greater than baseline.

In summary, an improvement in return vane performance has been achieved with the CR-1 geometry, but this gain is accompanied by a decline in diffuser performance. To improve the overall performance of the return passage, the gains in the return vane should be maintained, while the performance of the diffuser and return bend improved. To improve the diffuser and return bend performance, the extent of the separation region must be reduced without introducing other detrimental flow features.

4.3 Discussion of CR-2 Calculation Results

The cumulative loss coefficient in CR-2 is 10% lower than baseline, corresponding to approximately 0.6 points higher polytropic stage efficiency. A 20% reduction in return vane losses is achieved relative to the baseline, and there is an improvement in diffuser performance relative to CR-1, with a loss coefficient only 6% greater than baseline rather than 31%. Performance in the return bend is also improved with a 26% lower loss coefficient than baseline. Losses in the 90° bend increase by 18%, due

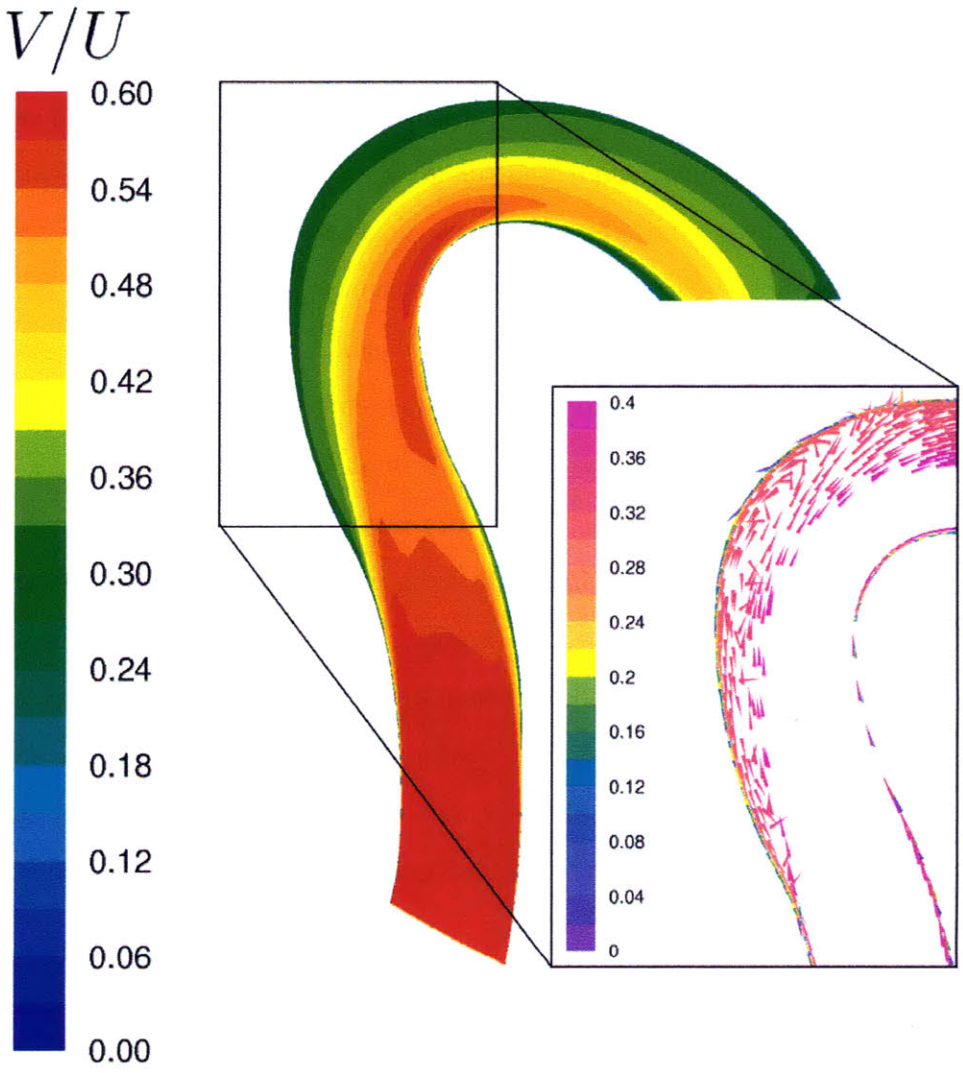

Figure 4-27: Contours of velocity magnitude in the CR-1 diffuser and return bend. The vector detail shows the separation region along the shroud in the diffuser and return bend.

Table 4.4: Change in loss coefficient between CR-2 and baseline return passages from three-dimensional calculations.

Component	$\Delta\zeta$
Diffuser	$\uparrow$6%
Bend	$\downarrow$26%
Vane	$\downarrow$20%
90°	$\uparrow$18%
CUMULATIVE	$\downarrow$10%

to separation, but it is expected that this can be remedied in subsequent designs by applying the design concepts used to eliminate separation at the exit of the return bend. Individual component loss coefficients are summarized in Table 4.4.

4.3.1 Flow Features and Loss Mechanisms in CR-2

The 20% reduction in losses from baseline in the CR-2 return vane is, as in CR-1, due to reduced separation at the return vane inlet, as well as reduction in leading edge incidence angle, shown in Figure 4-24. Figures 4-28 and 4-29 show contours of radial velocity and entropy production rate for the passage cross sections at intervals of 20% chord from the return vane leading edge to trailing edge. Reverse flow at the 0% chord station is isolated to a small region on the hub near the return vane blade. Between the 20% chord and 100% chord stations, a region of low velocity flow is present on the blade suction side. Small regions of high loss, associated with mixing of the separated flow and the core, are present at 20% chord and 40% chord stations, but the overall return vane losses are reduced from baseline.

In Figure 4-24 there is positive incidence between 0-20% and 40-100% span of the return vane in CR-1 that leads to increased losses[3], but in CR-2 there is positive incidence only between 0-10% span. However, the momentum flux in the CR-1 return vane is 4.0% and 8.7% lower than in CR-2 at the 0% and 20% chord stations, respectively, due to the wider CR-1 return vane channel, which leads to lower entropy production per unit area. Thus, although there are 20% lower return vane losses compared with the baseline in CR-1 and CR-2, a greater reduction in losses may be

[3]Personal communication from Dr. M. V. Casey

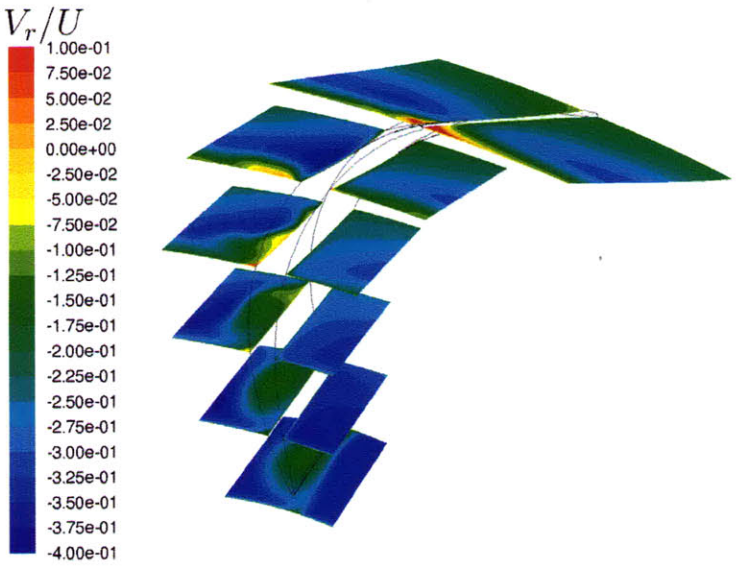

Figure 4-28: Contours of radial velocity on passage cross sections in the CR-2 return vane.

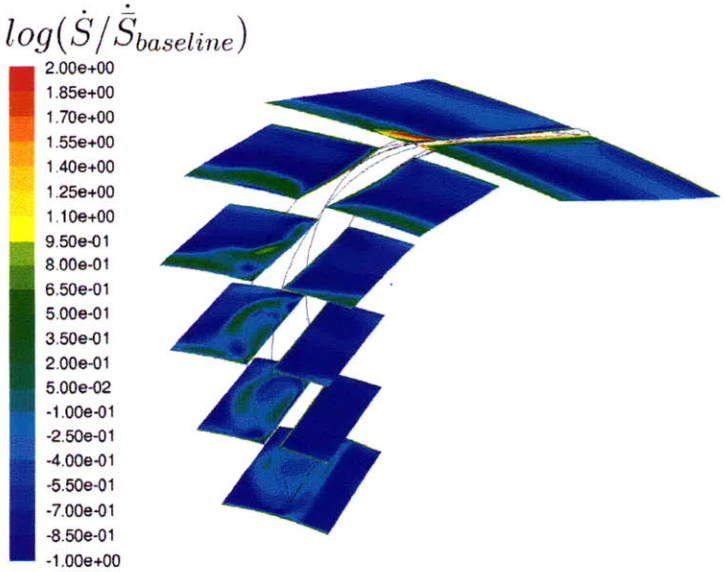

Figure 4-29: Contours of $log(\dot{S}/\dot{\bar{S}}_{baseline})$ on passage cross sections in the CR-2 return vane.

achieved if reduced momentum flux in the return vane and low incidence can both be realized.

Losses in the CR-2 diffuser and return bend are both lower than in CR-1 and CR-2 exhibits no separation in the diffuser or return bend. Contours of velocity magnitude in the CR-2 diffuser are shown in Figure 4-30. The detailed vector plot in Figure 4-30 confirms that there is no separation along the shroud in the diffuser or return bend, and hence lower blockage and freestream velocity. The lower freestream velocity results in lower boundary layer dissipation, an important loss mechanism in the diffuser and return bend. The momentum flux at the apex of the bend is 10.0% lower than baseline, despite 6.7% lower physical channel area.

There are increased losses in the 90° bend from separation on the shroud surface, which account for 12.7% of the overall losses in CR-2. Figure 4-31 shows contours of velocity magnitude at mid-pitch in the CR-2 90° bend. There is a separation region at the end of the bend on the shroud surface (seen as blue in Figure 4-31). In the design of CR-2, little attention was paid to the features of the 90° bend, as these contributed relatively little to the overall baseline and CR-1 losses. With additional design effort the methods used to mitigate separation in the return bend are expected to have the potential for providing performance in the 90° bend at the baseline level, resulting in an overall return passage loss coefficient more than 10% lower than the baseline.

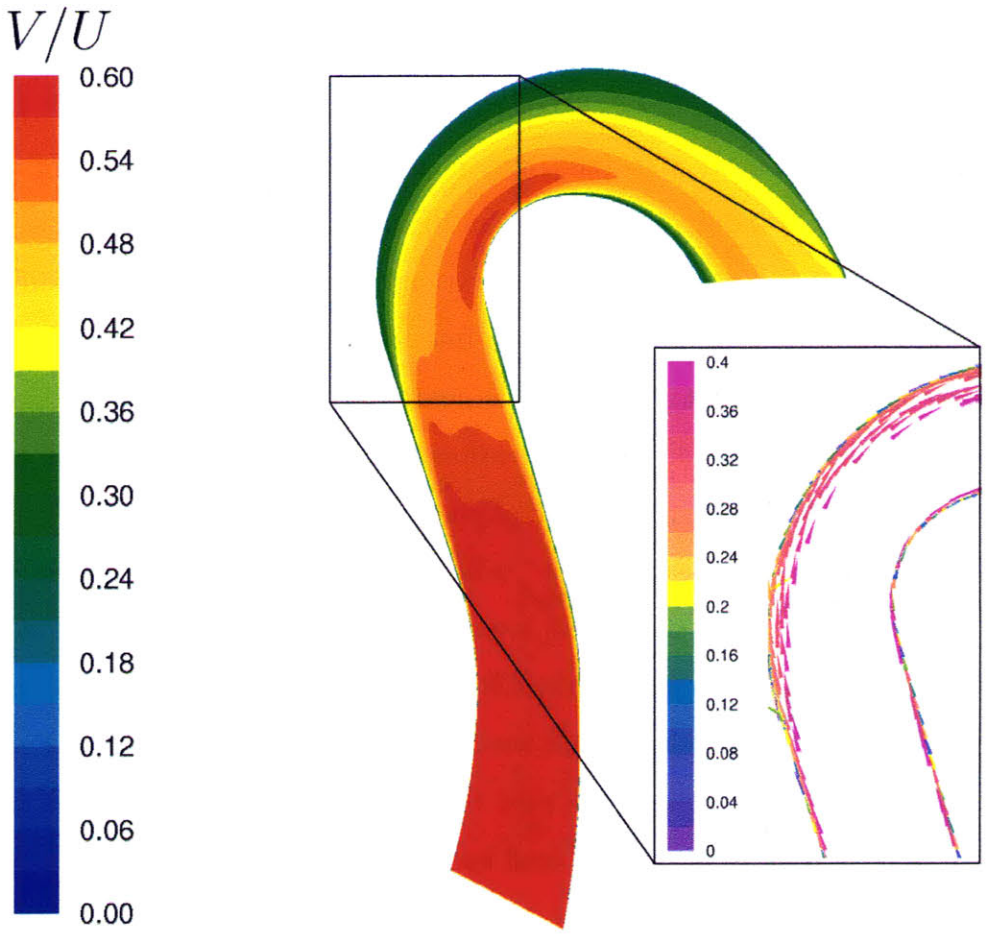

Figure 4-30: Contours of velocity magnitude in the CR-2 diffuser and return bend. The velocity vector detail in the inset shows fully attached flow along the shroud in the diffuser and return bend.

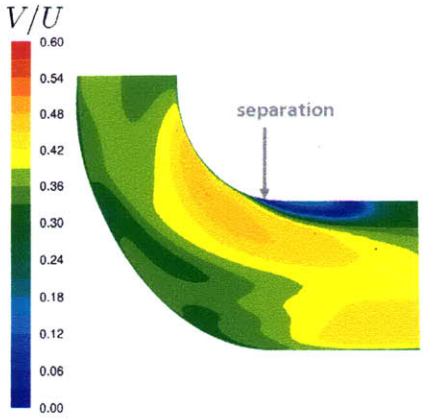

Figure 4-31: Contours of velocity magnitude in the CR-2 90° bend.

Chapter 5

Assessment of Return Passage with Modified Diffuser Inlet Geometry

To address the fourth research question outlined in section 1.3 we investigated the performance of a return passage that was not subject to the baseline diffuser inlet conditions and the geometry which all previous designs shared. In this investigation the diffuser inlet geometry was modified based on experience gained through development of the previous designs. The objective was not to develop an optimal return passage or stage design, but rather to assess whether further reduction in return passage losses might be achieved with modified diffuser inlet geometry and flow conditions. As such the computations did not consider the properties of the impeller required to achieve the modified diffuser inlet flow.

As described below, reduction of losses in the diffuser, return bend and return vane are achieved by modifying the diffuser inlet. However, the modified diffuser inlet flow may imply greater losses in the impeller and these must be balanced against the gains in the return passage. It is therefore suggested that future work focus on developing the impeller and return passage together.

We next describe the new diffuser inlet geometry and boundary conditions. The new candidate return passage geometry is then discussed and the flow field and losses analyzed.

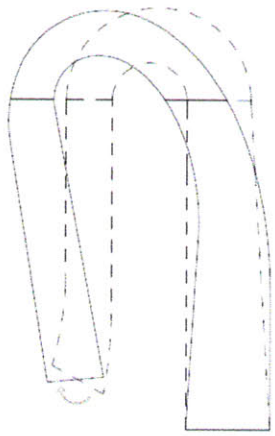

Figure 5-1: FD-1 meridional geometry.

5.1 Diffuser Inlet Geometry

Calculations of the CR-1 and CR-2 candidate return passages showed that losses in the diffuser were reduced with straight walls. To further reduce losses in the diffuser from the baseline level, and to maintain the increased axial extent of the CR-1 and CR-2 designs, straight, leftward swept walls are used, as shown in Figure 5-1. The diffuser inlet is rotated such that the flow normal to the inlet is directed parallel to the diffuser walls. The axial width of the diffuser inlet is adjusted to ensure the mass flow and momentum flux is kept the same as baseline. The series of return passages exhibiting this "flipped" diffuser inlet arrangement are hereafter denoted by 'FD'.

5.2 Diffuser Inlet Profile

The diffuser inlet conditions for the FD series return passages are based on the baseline diffuser inlet conditions. The mass flow was kept the same as the baseline mass flow. Figure 5-2 shows a close-up of the FD diffuser inlet overlaid on the baseline diffuser inlet. The baseline inlet, (ie. A to B) and the FD inlet (ie. C to D) were each divided into 101 sections at which a value of P_t, T_t, k, ω and flow angle was specified. The values of P_t, T_t, k and ω specified at each of the 101 FD sections were kept the same as the value of the corresponding section of the baseline inlet.

At the Mach numbers of interest, which exceed 0.7 near the shroud, the flow

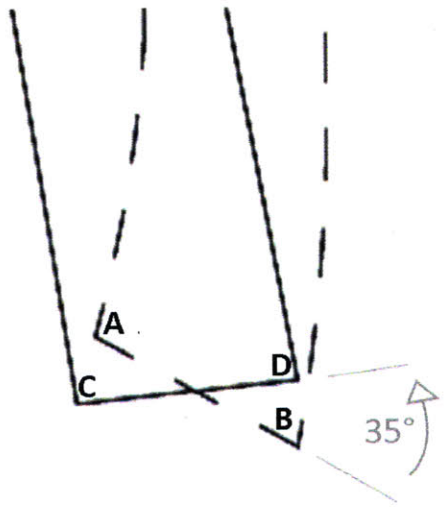

Figure 5-2: Detail view of baseline (A to B) and FD (C to D) diffuser inlet geometry.

angle varies with radius and there is a difference between the baseline inlet and the FD inlet. To calculate the flow angle for the FD configuration, the area ratio of the corresponding baseline and FD sections (from the 101 sections mentioned earlier) was assumed to be equal to the radius ratio. The corrected flow, Mach number and density at each FD inlet section were calculated from the baseline corrected flow and the area ratio, assuming isentropic flow. The ratio of radial to tangential velocity, and hence the flow angle in the r-ϑ plane, at each FD inlet section was calculated from the density ratio as:

$$(\frac{U_r}{U_\theta})_{FD} = (\frac{U_r}{U_\theta})_{baseline} \frac{\rho_{baseline}}{\rho_{FD}}. \tag{5.1}$$

The angle between the radial and axial components of velocity was set to ensure the velocity in the r-z plane was normal to the diffuser inlet for each section.

Once the diffuser inlet profile was specified in terms of the non-dimensional span, the physical width of the FD diffuser inlet was adjusted (by trial and error) until the momentum flux through the FD inlet was within 0.5% of the momentum flux through the baseline inlet.

5.3 Geometry with Modified Diffuser Inlet (FD-1)

The FD-1 diffuser inlet is rotated by 35° from the baseline and has a 9.2% greater axial extent. The straight diffuser walls are swept left to increase the axial extent of the return bend. The outer portion of the return vane is also angled towards the downstream stage to further increase the axial extent. Similar to PD-H, a constant radius of curvature is used through the first half of the return bend, followed by decreasing curvature in the remainder of the bend. The "pinch" at the entrance to the return bend is also carried over from PD-H, but is more severe in FD-1, at 18% of diffuser width. The return bend curvature is continued through the first half of the return vane, allowing a more gradual transition from the 180° bend to the straight return vane portion. The return vane leading edge is at the same radial location as baseline.

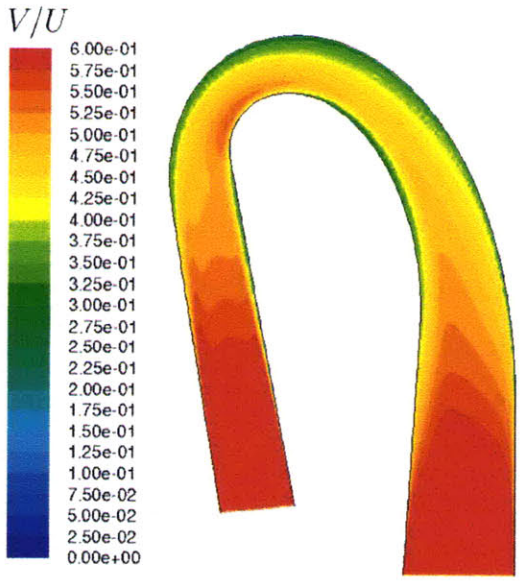

Figure 5-3: Contours of velocity magnitude from an axisymmetric calculation of flow in FD-1.

Figure 5-3 shows the FD-1 meridional geometry and contours of velocity magnitude from an axisymmetric calculation. There is no separation in the diffuser or return bend. The region of high velocity flow on the hub in the return bend is smaller than in the baseline. Because there is no curvature in the diffuser, the exit width

is increased, not including the "pinch", without triggering separation, and there is 5.5% lower peak velocity in the return bend compared with the baseline. Figure 5-4 shows that the pressure rise coefficient in the axisymmetric calculation, as a function of meridional distance, is greater than the baseline through the diffuser.

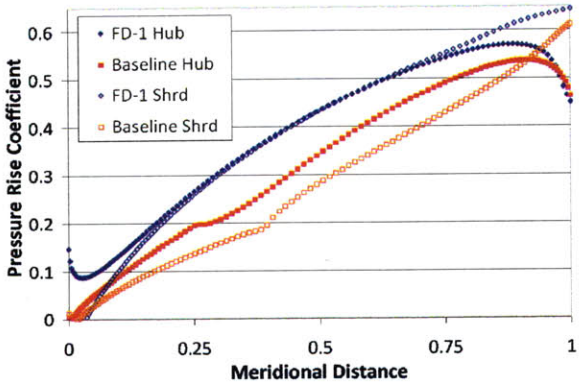

Figure 5-4: Pressure rise coefficient through the diffuser from an axisymmetric calculation of flow in FD-1.

As in CR-1 and CR-2, the FD-1 leading edge lean angle was selected to match the flow angle, based on the axisymmetric calculations. Figure 5-5 shows the calculated flow angle across the span at the leading edge radial station for FD-1 and the baseline return passage. The leading edge metal angle is a plotted as a dashed line from 35° on the hub to 25° on the shroud.

5.4 Discussion of FD-1 Three-dimensional Calculation Results

The cumulative loss coefficient in FD-1 is 27% lower than baseline. Higher pressure rise and no streamline curvature in the diffuser leads to 8% lower losses in the diffuser, as well as reduction in losses in the return bend and return vane. The return bend loss coefficient is 48% lower than baseline and the return vane loss coefficient is 35% lower. The 90° bend loss coefficient is 8% higher than baseline, but it is expected that this could be reduced in subsequent designs. Individual component loss coefficients are summarized in Table 5.1.

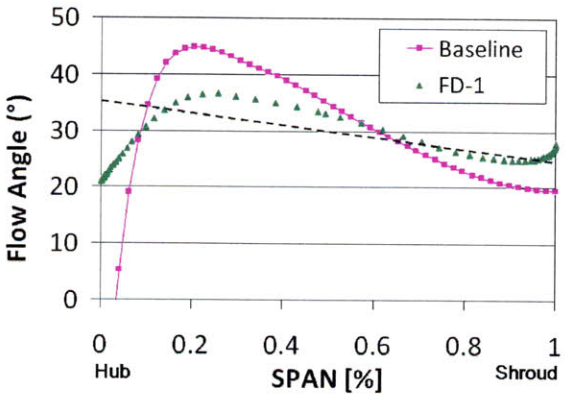

Figure 5-5: Flow angle across the span at the return vane leading edge from axisymmetric calculations. The FD-1 leading edge metal angle profile is shown as a dashed line.

Table 5.1: Change in loss coefficient in three-dimensional calculation of FD-1 and baseline return passage.

Component	$\Delta\zeta$
Diffuser	$\downarrow$8%
Bend	$\downarrow$48%
Vane	$\downarrow$35%
90°	$\uparrow$8%
CUMULATIVE	$\downarrow$27%

5.4.1 Flow Features and Loss Mechanisms in FD-1

Losses in the diffuser are primarily from boundary layer dissipation. As described above, the diffuser exit width, not including the "pinch", is larger than in the baseline, resulting in higher pressure rise in the diffuser, a reduction in velocity, and lower boundary layer entropy production per unit area. In this configuration the momentum flux upstream of the pinch, near 75% through the diffuser, is 3.8% lower than baseline and there is no streamline curvature in the diffuser.

Though the axial width of the FD-1 diffuser exit is 5% smaller than in the baseline, the "pinch" maintains fully attached flow in the diffuser and return bend, resulting in 0.5% lower momentum flux at the inlet to the return bend and 5.4% lower peak velocity near the hub. The more uniform flow manifests in 6.6% less momentum flux midway through the return bend in FD-1 compared with baseline, despite 17% less physical channel area. The reduced entropy production per unit area through the return bend is combined with lower losses near the return bend exit due to less separation and lower leading edge incidence angle across the span, shown in the plot of incidence angle across the span, Figure 5-6.

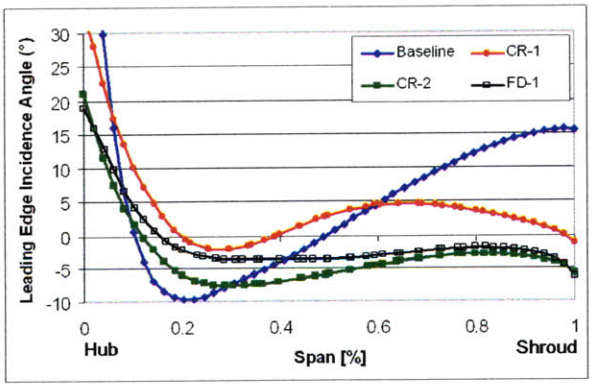

Figure 5-6: Incidence angle across the span at the return vane leading edge.

The reduced separation near the return bend exit and lower leading edge incidence also leads to reduced losses in the return vane. Figures 5-7 and 5-8 show contours of radial velocity and entropy production rate for the passage cross sections at intervals of 20% chord from the return vane leading edge to trailing edge. Reverse flow is present in a small region near the intersection of the vane pressure side and hub wall

at the 0% chord station, as well as where the flow accelerates around the return vane leading edge, but the flow is attached by the 20% chord station. A region of low velocity flow is present on the vane suction side between the 40% and 100% chord stations, with regions of high loss at the 40% and 60% chord stations. However there is less reverse flow, and less loss from mixing of the secondary and core flows in the FD-1 return vane, compared with the baseline return vane (see Figures 3-8 and 3-9.)

The increase in losses in the 90° bend is due to separation on the shroud surface and this additional loss needs to be addressed through additional tailoring of the 90° bend.

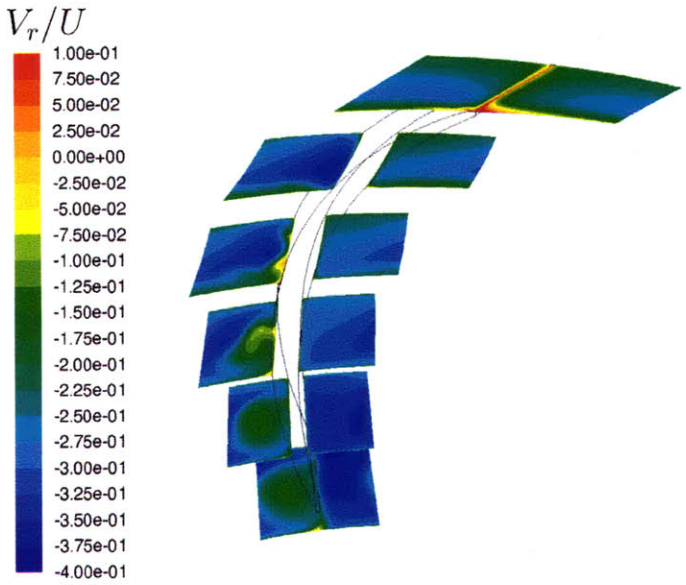

Figure 5-7: Contours of radial velocity on passage cross sections in the FD-1 return vane.

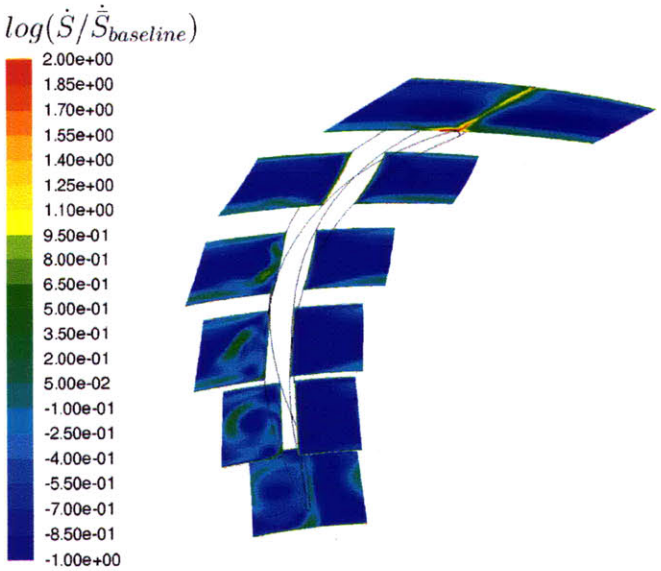

Figure 5-8: Contours of $log(\dot{S}/\dot{\bar{S}}_{baseline})$ on passage cross sections in the FD-1 return vane.

Chapter 6

Summary and Future Work

An assessment of flow and losses in a compact multistage centrifugal compressor return passage is presented along with the conceptual development of candidate improved performance return passages. The main points of the thesis and the recommendations for future work are summarized below.

6.1 Summary

A series of calculations of return passages have been carried out. Flow features which contributed losses in the baseline return passage were found to include separation on the shroud near the beginning of the return bend, separation on the hub near the exit of the return bend and non-zero incidence angle at the leading edge of the return vane.

Based on the identified loss mechanisms, return passage concepts were assessed using a combination of axisymmetric and three-dimensional calculations. Meridional geometry modifications, including an increase in the axial extent of the return bend, decreasing curvature in the latter half of the return bend, "pinching" the channel at the exit of the diffuser, and reducing the area ratio in the return bend were shown to eliminate separation on the shroud in the return bend and reduce separation on the hub at the exit of the return bend. Incidence angle was reduced by adding lean to the return vane leading edge, based on flow angles calculated in axisymmetric

calculations. The resulting return passage concept, denoted CR-2, exhibits a 10 % reduction in overall loss coefficient. It is expected that further reductions in loss coefficient can be achieved.

A return passage with modified diffuser inlet geometry, denoted FD-1, was developed and analyzed to assess the potential for further reductions in return passage losses if the diffuser inlet geometry is modified. The properties of the impeller required to achieve the modified inlet flow were not considered. The diffuser inlet was rotated to enable straight diffuser walls which are angled towards the upstream stage. Overall loss coefficient was reduced by 27% from baseline. It is likely that larger improvements can be achieved but these must be balanced against potential changes of impeller efficiency. It is thus suggested that an integrated development effort for the impeller and return passage be pursued.

6.2 Recommendation for Future Work

The intent of this thesis was to develop concepts for improved return passages. There is still much work left to be done to turn the concept into a realizable return passage design. It is expected that return passage losses can be reduced more than 10% from baseline, even with fixed diffuser inlet conditions. Some design features from FD-1 can be applied, including a more severe "pinch" at the diffuser exit, and continued curvature in the outer half of the return vane.

An understanding of the qualitative effect of geometry changes was gained, but it would be useful to define the link between geometry and return passage losses in a more quantitative manner. A parametric study of return passage losses which considers features such as return bend axial extent, "pinch" severity at diffuser exit, width scheduling, and continuation of curvature in the return vane is suggested.

Other modifications not considered in this thesis should also be investigated. A curved, 'S' shaped return vane which enables further extension of the return bend is one example.

In section 5 it was shown that a reduction in the return passage losses can be

achieved with modified diffuser inlet geometry and flow, but no consideration was given to the required impeller design or losses in the impeller. It is thus recommended that the impeller and return passage be developed together.

Much of the work in this thesis followed a heuristic, trial and error approach. While this was effective for initial conceptual exploration, a more methodical design approach may prove valuable in future design efforts. One such approach that may be effectively employed in future work to refine the design of the return passage is an adjoint method [21].

Finally, the operational range of any new compressor stage is important, and design limitations may be imposed to ensure sufficient range. The stable operating range of compressors employing the new return passage concept should thus be investigated.

Appendix A

Upstream Influence of Return Vane

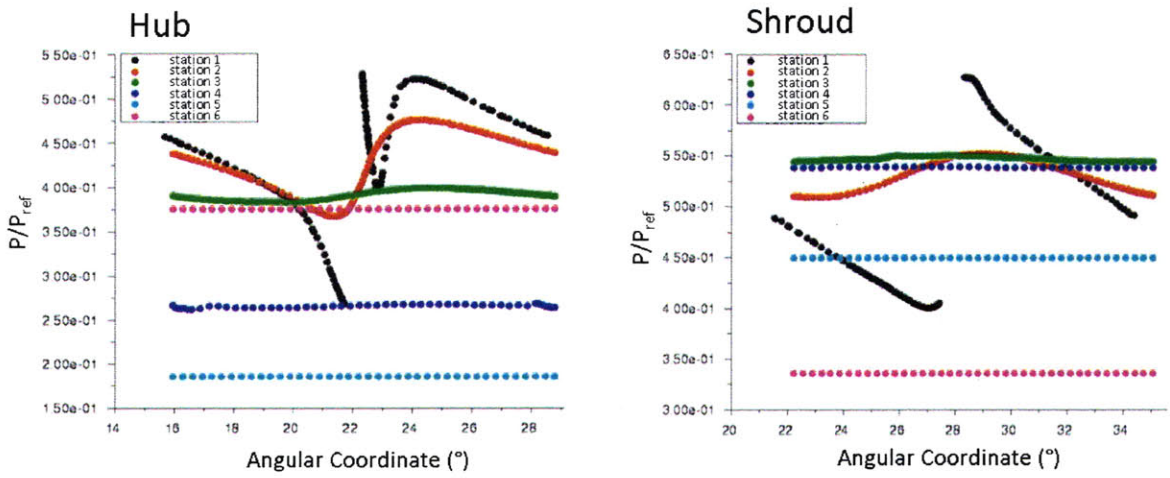

Figure A-1: Pressure distributions on the hub (left) and shroud (right) surfaces upstream of the return vane leading edge in CR-1.

As described in section 2.2.3 the upstream influence of the return vane on the flow field in the return bend and diffuser was investigated to validate the use of axisymmetric calculations as a design tool. Figure A-1 shows pitchwise pressure distributions on the CR-1 hub and shroud surfaces at the six locations shown in Figure A-2. The black traces in Figure A-1 show a jump in static pressure across the return vane leading edge at station 1. The disturbance in static pressure rapidly decays upstream of the return bend. No appreciable pitchwise pressure disturbance is seen at stations 3-6 on the shroud or stations 4-6 on the hub.

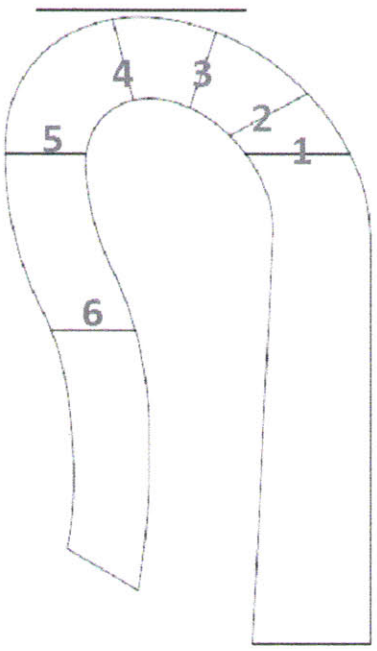

Figure A-2: Schematic showing location of six pressure distributions in CR-1. The horizontal bar at top shows the pitch length.

A comparison of the return bend flow field in the CR-1 geometry from a three-dimensional calculation with return vane blades and an axisymmetric calculation with no blades in Figure A-3 confirms that separation occurs at approximately the same location on the hub surface. Because the objective of the axisymmetric calculations was to quickly assess the effect of alternative meridional geometries on separation, it was determined that axisymmetric calculations would provide valuable insight despite having no return vane blades.

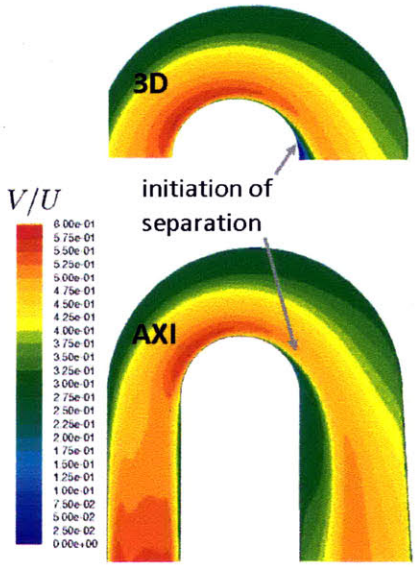

Figure A-3: Contours of velocity magnitude near the return bend from a three-dimensional and an axisymmetric calculation of the flow in CR-1.

Bibliography

[1] K. H. Lüdtke, *Process Centrifugal Compressors*. Springer-Verlag, 2004.

[2] N. A. Cumpsty, *Compressor Aerodynamics*. Harlow, Essex, England: Longman Scientific & Technical, 1989.

[3] J. Masutani, J. Koga, and Y. Kawashima, "Development of high-performance, high-speed, compact centrifugal compressor stage," Tech. Rep. Vol.36 No.1, Mitsubishi Heavy Industries, Ltd., February 1999.

[4] H. Simon and E. Rothstein, "On the development of return passages of multistage centrifugal compressors," in *Applied Mechanics, Bioengineering and Fluids Engineering Conference*, (Houston, Texas, USA), ASME FED, 1983.

[5] Y. Inoue and T. Koizumi, "An experimental study on flow patterns and losses in return passages for centrifugal compressor," in *Applied Mechanics, Bioengineering and Fluids Engineering Conference*, (Houston, Texas, USA), ASME FED, 1983.

[6] R. Furst, "Experimental evaluation of diffusing crossover systems for a high-pressure liquid hydrogen pump," in *Applied Mechanics, Bioengineering and Fluids Engineering Conference*, (Houston, Texas, USA), ASME FED, 1983.

[7] S. Y. Meng and E. D. Jackson, "The continuous diffusion crossover system design," in *Applied Mechanics, Bioengineering and Fluids Engineering Conference*, (Houston, Texas, USA), ASME FED, 1983.

[8] W. Fister, G. Zahn, and J. Tasche, "Theoretical and experimental investigations about vaneless return channels of multi-stage radial flow turbomachines," in *ASME paper 82-GT-209*, 1982.

[9] L. J. Lenke and H. Simon, "Numerical simulation of the flow through the return channel of multi-stage centrifugal compressors," in *ASME paper 98-GT-255*, (Stockholm, Sweden), pp. 10–19, 1998.

[10] C. Aalburg, A. Simpson, M. B. Schmitz, V. Michelassi, S. Evangelisti, E. Belardini, and V. Ballarini, "Design and testing of multi-stage centrifugal compressors with small diffusion ratios," in *Proceedings of ASME Turbo Expo 2008: Power for Land, Sea and Air*, no. GT2008-51263, (Berlin, Germany), 2008.

[11] C. Aalburg, A. Simpson, M. B. Schmitz, V. Michelassi, S. Evangelisti, E. Belardini, and V. Ballarini, "Extension of the stator vane upstream across the 180° bend for a multistage radial compressor stage," in *Proceedings of ASME Turbo Expo 2009: Power for Land, Sea and Air*, no. GT2009-59522, (Orlando, Florida, USA), 2009.

[12] A. Veress and R. Van den Braembussche, "Inverse design and optimization of a return channel for a multistage centrifugal compressor," *ASME Journal of Fluids Engineering*, vol. 126, pp. 799–806, September 2004.

[13] F. R. Menter, "Improved two-equation k-omega turbulence models for aerodynamic flows," Tech. Rep. TM 103975, NASA, 1992.

[14] ANSYS, Inc., *ANSYS FLUENT 12.0 Theory Guide*, April 2009.

[15] C. J. Sagi and J. P. Johnston, "The design and performance of two-dimensional, curved diffusers," *ASME Journal of Basic Engineering*, pp. 715–731, December 1967.

[16] P. E. Smirnov and F. R. Menter, "Sensitization of the sst turbulence model to rotation and curvature by applying the spalart-shur correction term," *Journal of Turbomachinery*, vol. 131, October 2009.

[17] O. B. Adeyinka and G. F. Naterer, "Modeling of entropy production in turbulent flows," *Journal of Fluids Engineering*, vol. 126, pp. 893–899, November 2004.

[18] M. V. Casey, "The industrial use of cfd in the design of turbomachinery," tech. rep., Fluid Dynamics Laboratory, Sulzer Innotec AG, 1994.

[19] W. N. Dawes, "A simulation of the unsteady interaction of a centrifugal impeller with its vaned diffuser: Flow analysis," *ASME Journal of Turbomachinery*, vol. 117, pp. 213–222, April 1995.

[20] E. M. Greitzer, C. S. Tan, and M. B. Graf, *Internal Flow: Concepts and Applications.* Cambridge University Press, 2004.

[21] Q. Wang, D. Gleich, A. Saberi, N. Etemadi, and P. Moin, "A monte carlo method for solving unsteady adjoint equations," *Journal of Computational Physics*, vol. 227, pp. 6184–6205, June 2008.